1-1-2008

Biomedical applications of photoacoustics for thermal therapy

Robin Castelino
Ryerson University

BIOMEDICAL APPLICATIONS OF PHOTOACOUSTICS FOR THERMAL THERAPY

by

Robin Castelino

B. Eng., Ryerson University, Toronto, 2005

A thesis

presented to Ryerson University

in partial fulfillment of the

requirements for the degree of

Master of Applied Science

in the Program of

Electrical and Computer Engineering

Toronto, Ontario, Canada, 2008

AUTHOR'S DECLARATION

I hereby declare that I am the sole author of this thesis. I authorize Ryerson University to lend this thesis to other institutions or individuals for the purpose of scholarly research.

ROBIN CASTELINO

I further authorize Ryerson University to reproduce this thesis by photocopying or by other means, in total or in part, at the request of other institutions or individuals for the purpose of scholarly research.

ROBIN CASTELINO

Biomedical Applications of Photoacoustics for Thermal Therapy

Robin Castelino, Master of Applied Science, 2008

Department of Electrical and Computer Engineering, Ryerson University

Abstract

This work demonstrates the feasibility of Photoacoustic tomography (PAT) and real-time photoacoustic (PA) monitoring using a single transducer prototype system to detect and/or monitor tumour growth using low absorbing targets embedded in turbid phantom and thermal lesions in tissue. A single transducer PA prototype system is built utilizing a laser system producing light in the near infra-red while ultrasonic transducers detects the PA pressure waves generated. The ability to image tissue using PAT is initially demonstrated using gelatin phantoms with targets of similar optical properties to native and coagulated prostate tissue. Next, lesions in bovine muscle tissue and bovine liver are also imaged demonstrating the effectiveness of PAT to detect lesions during thermal therapy (TT). Selective imaging is shown by varying the optical wavelength to preferentially absorb light and target specific structures which in turn produce high contrast after image reconstruction. Finally, the capability of using PA to monitor TT is explored by measuring the changes in the optical and mechanical properties of tissue equivalent albumen phantoms as a function of thermal dose on PA signals, thereby demonstrating the real time capability of this modality to monitor TT.

ACKNOWLEDGEMENTS

I would like to thank my parents and sister for their love, care, support and constant understanding.

I would like to thank my co-supervisors Dr. Michael Kolios and Dr. William Whelan for their guidance and advice. I am very grateful that you gave me the opportunity.

I would also like the thank Arthur Worthington for his expertise in assisting me build my experimental setup; Behrouz Soroushian for all the optics knowledge and help that I most definitely needed; Barry Vuong for his LabView programming knowledge and Marian de Silva for her creative help with illustrations. It would have been much more painful without all the help. Thank you.

Finally, I would like to thank all the ultrasound/optics lab members: Matthew Rodrigues, Omar Falou, Madhu Jain, Nazanin Nayebi, Ahmed El Kaffas and Rachel Guha – who made the physics environment fun, humourous and stimulating. Thank you for making the last two years extremely memorable.

TABLE OF CONTENTS

LIST OF FIGURES

LIST OF TABLES

NOMENCLATURE

α_{th}	thermal diffusivity [m^2/s]
$A(\mathbf{r})$	optical energy deposition at position $\boldsymbol{r}$
β	thermal coefficient of volume expansion [K^{-1}]
c	speed of sound in a medium [m/s]
C_p	heat capacity at constant pressure [J/gK]
d	effective penetration depth [cm]
d_c	characteristic dimension of the heated region [m]
$D(t \cdot c)$	transducer impulse responses in the spatial domain
$\delta(t)$	delta function
$\Delta P(z)$	change in pressure at depth z [Pa]
g	anisotropy factor
Γ	Grüneisen parameter
$H(\boldsymbol{r},t)$	radiation deposited at position $\boldsymbol{r}$ at time t [J]
$I(r)$	reconstructed image
$I(t)$	shape of the irradiation pulse
$L(t \cdot c)$	laser pulse in spatial domain
M	bulk modulus [Pa]
n	index of refraction
$p(\boldsymbol{r},t)$	photoacoustic pressure at position $\boldsymbol{r}$ at time t [Pa]
$\Psi(z)$	laser fluence at depth z [J/cm2]
$\boldsymbol{r}_0$	detection radius
R_d	diffuse reflectance
ρ	density [g/cm^3]
$S(r)$	optical structure of tissues
t_{43}	thermal dose, equivalent time at 43°C [eq. min]
t_N	peak-to-peak time of photoacoustic N-shaped profile [s]
T_c	collimated transmittance

T_d	diffuse transmittance
τ_s	stress confinement time [s]
τ_{th}	thermal confinement time [s]
μ_a	absorption coefficient [cm^{-1}]
μ_{eff}	effective attenuation coefficient [cm^{-1}]
μ_s	scattering coefficient [cm^{-1}]
μ'_s	reduced scattering coefficient [cm^{-1}]

ABBREVIATIONS

CT	Computer Tomography
CW	Continuous Wave
DIS	Double Integrating Sphere
EM	Electromagnetic
FD	Frequency Domain
IAD	Inverse Adding Doubling
MC	Monte Carlo
MITT	Minimally Invasive Thermal Therapy
MPE	Maximum Permissible Exposure
MRTI	Magnetic Resonance Temperature Imaging
NIR	Near Infra-red
OPO	Optical Parametric Oscillator
PA	Photoacoustic
PAT	Photoacoustic Tomography
PET	Positron Emission Tomography
PRF	Pulse Repetition Frequency
RBP	Radial Back-Projection
TT	Thermal Therapy

1 Introduction

1.1 Overview

The photoacoustic (PA) effect refers to the generation of acoustic waves by the absorption of electromagnetic (EM) radiation. This effect has been known since the discovery by Bell *et al.* on the effect of sunlight on a selenium cells [1]. Not until the advent of lasers was it feasible to efficiently generate acoustic waves in biological media [2] however since then, much theoretical and experimental work on photoacoustics for biological imaging has been conducted [2-8].

There currently are two modes to create a PA effect. A frequency domain (FD) method where the excitation source is by a continuous wave (CW) laser [9] and a pulsed method, introduced in the late 1970's [2], whereby the deposition of energy is by a pulsed laser. When a light source irradiates an absorbing medium, the absorbed energy is converted into heat by a photothermal interaction. This thermal expansion induces pressure transients which propagate through a medium giving rise to pressure waves typically with frequencies from 50kHz to 5MHz, depending on the size of the absorbing structures [10]. To effectively produce the photoacoustic effect, the condition of temporal confinement must be satisfied where the optical pulse duration must be shorter than the time required for the deposited energy to propagate away acoustically and thermally [2]. By its dual nature, PA imaging overcomes the poor resolution due to light scattering associated with pure optical imaging and the poor tissue contrast associated with ultrasound imaging [3].

The work presented in this thesis provides background on PA generation, detection and image reconstruction using only the pulsed PA method. The long term goal of the work is to use PA imaging to successfully guide and monitor thermal therapy (TT).

1.2 Optical Properties

There are two optical windows that allow light to penetrate relatively deep into biological tissues. They are between 600 – 1300 nm and 1600 – 1850 nm, the visible to near infra-red (NIR) and the mid infra-red, respectively. The former is of more interest because of the high contrast of blood and also since many laser sources are available in this range.

Optical properties in a turbid medium, such as tissue, are described by the absorption coefficient μ_a [cm^{-1}], the scattering coefficient μ_s [cm^{-1}] and the index of refraction n. Molecules that absorb photons such as hemoglobin and melanin are called chromophores. Differences in chromophore concentrations within tissues cause tissue-specific absorption coefficients values which are typically in the range of ~0.1cm^{-1} to ~ 10 cm^{-1} in the visible to NIR window [11]. Figure 1-1 shows the optical absorption in several biological tissues in as a function of wavelength [12].

The scattering of photons is caused by microscopic changes in the tissue refractive index. This effects the spatial distribution of the photons through the medium [13] and is expressed as the scattering coefficient, μ_s [cm^{-1}], which is related to probability of the number of scattering events per unit distance in a medium. The anisotropy factor, g, describes the directional probability of scattering. It ranges from -1

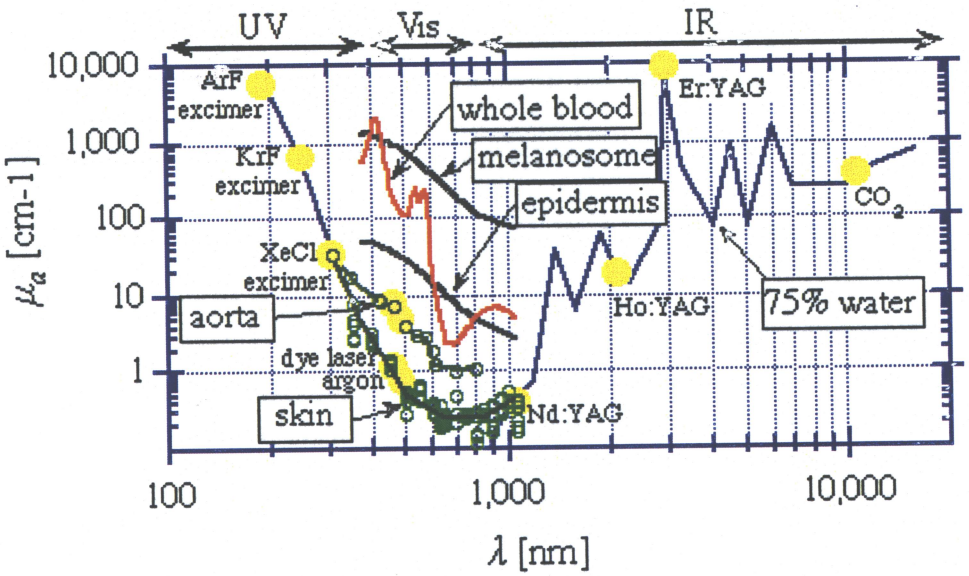

Figure 1-1: Absorption coefficients of several biological tissues at typical laser wavelengths [12]

to 1 where g = 1 describes total forward scattering, g = -1 indicates total backward scattering and g = 0 implies scattering about the backward and forward direction. The *reduced or effective scattering* coefficient μ_s' [cm^{-1}] incorporates both μ_s and g and is defined by:

$$\mu_s' = \mu_s(1-g) \tag{1.1}$$

In tissue, μ_s is typically ~100 cm^{-1} to ~250 cm^{-1} and g ~ 0.9 in the visible to near-IR region [11]. A notable characteristic in tissue is its strong scattering as compared to absorption. When scattering is much greater than absorption, as in tissue, the effective attenuation coefficient μ_{eff} [cm^{-1}] can be defined by:

$$\mu_{eff} = \sqrt{3\mu_a(\mu_a + \mu_s')} \tag{1.2}$$

This becomes a useful parameter as it describes the effective penetration depth, d, which is the reciprocal of μ_{eff} [11, 14]. The effective attenuation shows that in turbid media light penetration is dependent not only on absorption but also on scattering too. Tissue optical absorption and scattering is wavelength dependent which makes the penetration depth in tissues a function of wavelength. Within the visible and NIR region photons penetration in tissue can be up to several centimeters [11, 13].

Figure 1-2 shows Monte Carlo simulations of the behaviour of light in media with different optical properties. Light is focused downwards and is positioned so that it is incident on the surface of an infinitely long media. Figure 1-2(a) shows photon paths for a medium with low absorption and low scattering. As shown, the photon path is straight and the propagation of light deep as compared to Figure 1-2(b) where the photons are more highly absorbed and with low scattering causing only a small amount of photons to travel far from the point where they entered into the medium. However, due to the low scattering the photons that do travel further follow a straight path. Figure 1-2(c) illustrates an example of low absorption and high scattering. In this simulation, photons are not highly absorbed and therefore can travel significantly more. Due to the high scattering their path is very spread laterally out in all directions. The medium in Figure 1-2(d) is highly scattering, such that photons are quickly absorbed due to the nature of the medium and this prevents them from traveling far from the plane of incidence. It is apparent from these simulations that in the presence of high scattering, as in tissue, penetration depth will be limited. The anisotropy factor for all simulations is 0.9 and to increase readability, all photons traveling backwards past the past the plane of incidence are ignored.

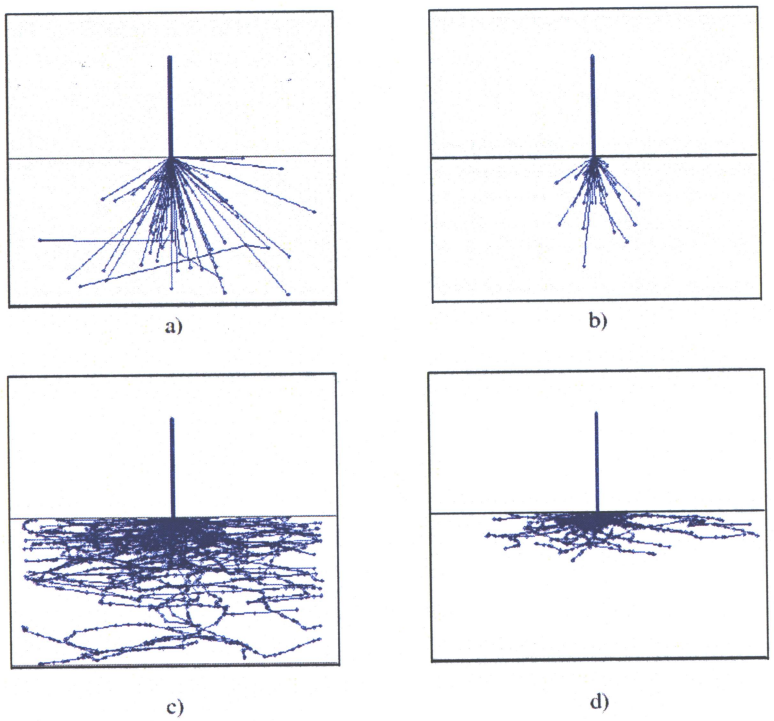

Figure 1-2: Monte Carlo simulation depicting the effect of optical absorption and scattering of light propagation in a medium. The images show the paths of individual photons traveling in a medium with: (a) low absorption and low scattering, (b) high absorption and low scattering, (c) low absorption and high scattering and (d) high absorption and high scattering

The PA pressure transients generated during PA imaging are proportional to the number of photons absorbed. Therefore, if the medium has a higher absorption coefficient a PA pressure wave with greater amplitude will result. Also, since tissue is highly scattering it can significantly effect the optical distribution of photons resulting within the medium thus affecting generation of PA waves.

1.3 Acoustic Properties

Acoustic properties of tissue influence how an acoustic wave travels once it is generated and also determines the characteristics of the wave in the medium. Speed of

sound, c, is the acoustic velocity in a medium. At 20°C, the speed of sound in water is 1480m/s while the mean speed of sound in soft tissue at 37°C is c = 1540m/s [15].

Sound propagation is dependant on acoustic scattering, refraction and attenuation. As waves propagate from one medium to another a portion of the energy is reflected which is determined by the acoustic impedance difference between two media. If two media have different speed of sounds, refraction will be experienced by the propagating wave, in a way similar to optical refraction.

The dominant loss mechanism of sound energy in tissues is attenuation which is primarily due to acoustic absorption which is dependent on frequency and temperature [15-17]. Attenuation is proportional to frequency and so with increased frequency the distance traveled by an acoustic wave before most of its energy is lost, is greatly lowered [18]. Losses also occur when the acoustic waves are scattered due to small size particles within a medium but, as opposed to light propagation, this effect is not as dominant. The mean ultrasound attenuation in soft tissue is ~0.6 dB cm^{-1} MHz^{-1} and at 3MHz the effective penetration depth is ~150mm [16, 17].

Low frequency ultrasound (<10MHz) typically has low scattering and can travel larger distances without being attenuated, however it is associated with longer wavelengths, thus limiting the size of objects that can be resolved. In comparison, high frequency ultrasound provides better resolution at the cost of greater attenuation and is limited to surface applications. PA imaging can be used with both high frequency and low frequency transducers to detect the pressure transients. The application determines the choice of transducer and it is left to the designer to optimally balance resolution with imaging depth. However, in PA imaging the acoustic wave travels only once between the

target and the detector, as opposed to ultrasound imaging (in pulse-receive mode) where the distance is twice

1.4 Safety

Exposure to EM radiation must be controlled for safety reasons. The safety limiting parameter is called the maximum permissible exposure (MPE) and is defined as the amount of EM radiation to which tissue may be exposed without hazardous effects or biological changes. The American National Standard (Z136.1-2000) tabulates the MPE for specific laser wavelengths from 180nm – 1mm and for different exposure durations [19]. MPE levels are a function of optical wavelength, exposure time and pulse repetition frequency and are expressed in terms of radiant exposure (J/cm^2) or irradiance (W/cm^2). The general rule of thumb is the longer the wavelength, the higher the MPE; and the longer the exposure time, the lower the MPE.

For exposure to a laser beam in the visible and NIR wavelength region (λ = 400nm – 1400nm)

$$MPE = \begin{cases} 200C_A \dfrac{mW}{cm^2} & 10s \le T \le 30000s \\ 1.1C_A T^{0.25} \dfrac{J}{cm^2} & 10^{-7}s \le T < 10s \\ 200C_A \dfrac{mJ}{cm^2} & 10^{-9}s \le T \le 10^{-7}s \end{cases} \tag{1.3}$$

where T is the exposure duration and where

$$C_A = \begin{cases} 1.0 & 400nm \le \lambda < 700nm \\ 10^{2(\lambda-0.7)} & 700nm \le \lambda < 1050nm \\ 5.0 & 1050nm \le \lambda \le 1400nm \end{cases} \quad (1.4)$$

Therefore, a CW laser source at 650nm will have a MPE of 20 mW/cm^2 compared to a single pulse with duration of 10ns which will have a MPE of 200 mJ/cm^2.

To calculate the MPE due to repetitive-pulse laser the pulse repetition frequency (PRF), the duration of any pulse groups, T, and the duration of a complete exposure, T_{max}, must be known in addition to the wavelength and the single pulse length. Using the minimum of the following three rules the MPE/pulse can be attained:

Rule 1: The single pulse limit: MPE_{SP} is limited by any single pulse during the exposure

Rule 2: The average power limit: MPE is limited by the duration of all pulse trains, t, divided by the number of pulses, n, for all exposure durations up to T_{max}

Rule 3: The repetitive pulse limit: MPE is limited by MPE_{SP} multiplied by a correction factor, $n^{(-0.25)}$, where n is the number of pulses during the exposure t_{max}

In a typical PA experiment and for a 650nm exposure with a PRF = 10Hz, T=10s and a pulse width of 10 ns the above three rules produce the following:

Rule 1: MPE_{SP} = 200 mJ/cm^2

Rule 2: MPE = 1.1 x $10^{0.25}$ = 2 J/cm^2. Therefore, MPE/pulse = 2/100 J/cm^2 = 20mJ/cm^2 where n = PRFx10 = 100 pulses

Rule 3: MPE/pulse = $n^{(-0.25)}$ x MPE_{SP} = $100^{(-0.25)}$ x 200 mJ/cm^2 = 63 mJ/cm^2

The MPE/pulse is therefore derived using Rule 2 and is limited to 20mJ/cm^2.

1.5 Photoacoustic Effect

In this work the PA generation is caused by a pulsed optical source delivering low levels of radiation that cause pressure transients due to thermoelastic expansion induced by a small temperature rise resulting from the absorbed energy deposition inside the tissue. For the PA effect to be produced efficiently during laser heating, the pulse duration must be shorter than two timescales. They are the *thermal relaxation time* and *stress relaxation time*. Thermal relaxation time is defined by [8]:

$$\tau_{th} = \frac{d_c^2}{\alpha_{th}} \tag{1.5}$$

where α_{th} [m^2/s] is the thermal diffusivity and d_c [m] is the characteristic dimension of the heated region of the structure of interest (e.g. absorber radius). Stress relaxation time is defined by [8]:

$$\tau_s = \frac{d_c}{c} \tag{1.6}$$

where c [m/s] is the speed of sound in the sample. When the laser pulse is much shorter than τ_{th} and τ_s the excitation is said to be in thermal and stress confinement respectively; such that heat conduction and stress propagation during laser heating are negligible thereby efficiently generating PA waves.

PA waves, like acoustic waves, propagate in three-dimensional space and can be described by the change in pressure $\Delta P(z)$ [20]:

$$\Delta P(z) = \Gamma \mu_a \Psi(z) \tag{1.7}$$

where Γ is the Grüneisen parameter, $\Psi(z)$ [J/cm^2] is the laser fluence at depth z and μ_a is the absorption coefficient of the optical absorber. The Grüneisen parameter, Γ, is a dimensionless quantity which represents thermoacoustic efficiency. It is a temperature dependent factor proportional to the fraction of thermal energy converted into mechanical stress and can be expressed as:

$$\Gamma = \frac{M\beta}{\rho C_P} = \frac{\beta c^2}{C_P} \tag{1.8}$$

where M [Pa] is the bulk modulus, ρ [g/cm^3] is density, C_p [J/gK] is the heat capacity at constant pressure and β [K^{-1}] is the thermal coefficient of volume expansion of the sample. At 20°C, Γ = 0.1 for water and aqueous solutions [21]. In comparison for fats, lipids, and oils, Γ = 12.7 and as such are the most efficient biological media for PA generation in the presence of chromophores that would absorb light [3]. Within the range of 4°C to 100°C in liquid water, the Grüneisen parameter can be expressed by the following [3, 22]:

$$\Gamma(T) = -0.0000236T^2 + 0.007T - 0.033 \tag{1.9}$$

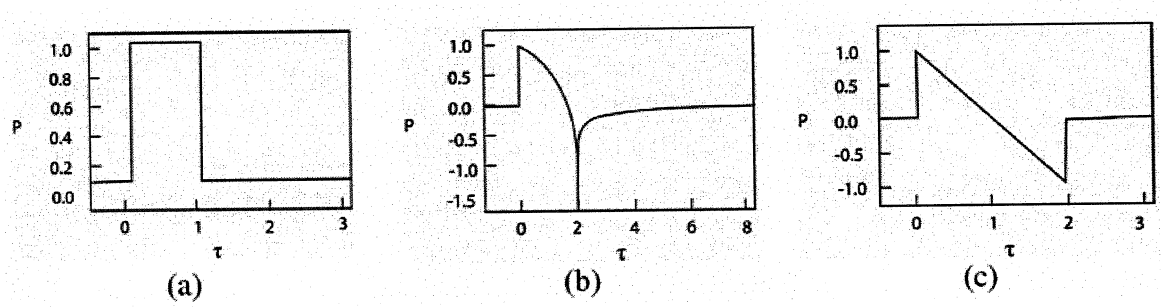

Figure 1-3: PA pressure *P* (in arbitrary units) vs. dimensionless retarded time τ for short pulse heating of optically thin (a) fluid layer (b) cylinder and (c) sphere [7]

where T is measured in degrees Celsius. It can therefore be seen that Γ changes from 0.194 at 37°C to 0.376 at 80°C which is a typical temperature reached during TT.

The induced acoustic waves travel through the medium where they can be detected. Analytical solutions for specific optically thin well defined geometries when heated with a short pulse have been reported by *Diebold et al.*, and their pressure profiles for are shown in Figure 1-3 [7]. When the excitation source produces a long Gaussian pulse, as in a practical case of a typical pulsed laser output, the profiles of these geometries are shown in Figure 1-4 [7]. In the cylindrical or spherical cases, the difference of peaks in the N-shape feature corresponds to the diameter of the absorber.

Equation (1.7) is only valid when the conditions of thermal and stress confinement are satisfied [8]. If this is not the case, the PA signal will be much weaker thereby causing the reconstructed PA image to lose both sensitivity and resolution due to the decreased SNR. Although there are many methods of detecting propagating acoustics waves, the most common method involves using wideband ultrasonic transducers which are sensitive to small vibrations across a large frequency range.

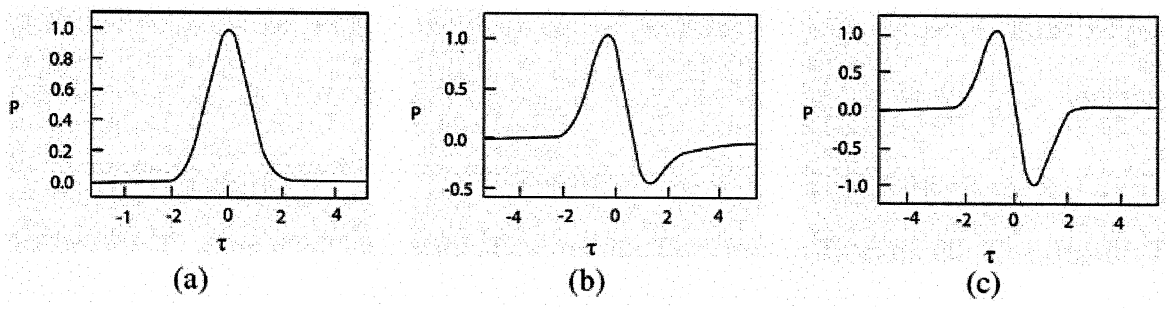

Figure 1-4: PA pressure *P* (in arbitrary units) vs. dimensionless time τ for heating by a long Gaussian pulse of (a) fluid layer (b) cylinder and (c) sphere [7]

1.6 Photoacoustic Tomography

Photoacoustic tomography (PAT) also called optoacoustic or thermoacoustic tomography in can be described as optically induced ultrasound imaging; however it is significantly different from traditional ultrasound imaging [2, 3]. The acoustic waves produced in PAT are broadband and generally have higher frequency content than traditional ultrasound. In pulse/echo ultrasound, the acoustic source is in the externally positioned transducer and the frequency content of the detected signals is primarily determined by the acoustic pulse used. The ultrasound images produced depend mainly on the acoustic frequency and contrast. In PAT, the acoustic waves are created within the tissue and primarily depend on the contrast between the optical and mechanical properties of the absorber and the surrounding media, thus enhancing the differences of the targeted tissue and surrounded media. The frequencies generated in PAT can be as high as 100MHz and are dictated by the absorber size [3] . Laser pulses directed at targeted tissue, at most, raise the temperature by a fraction of a degree; and like ultrasound, PAT has the benefit over positron emission tomography (PET), computer tomography (CT) and

x-ray imaging methods in that the acoustic waves produced are not created by ionizing radiation.

The advantage of PAT is that it possesses the benefits of optical and ultrasound imaging systems – good optical contrast and high spatial resolution. It inherently overcomes the problems of loss in resolution and sensitivity due to light scattering in pure optical imaging as well as poor tissue contrast and low SNR associated with pure ultrasound imaging [3, 23-25]. The induced acoustic signals exhibit the heterogeneity of optical absorption in the samples and reveal the different structure of tissues. For select wavelengths of light, the absorption coefficient of blood can be up to 10 times greater than that of the surrounding tissues [26] and due to the abnormal vasculature in malignant tumours, it has been reported that the absorption contrast between breast tumours and normal breast tissues can be as high as 300% [25, 27].

PAT can be performed using three detection modes: (i) forward mode, (ii) side mode and (iii) backward mode [3]. In forward and side modes, the laser irradiation and acoustic detection are not performed on the same surface of the tissue while in backward mode, the irradiation and detection share the same tissue surface. Forward mode requires the acoustic waves to propagate to the other side of the tissue and can be impractical in settings outside the laboratory. Side mode has been successfully used in breast cancer detection and small animal imaging [10, 28, 29]. Backward mode is least used but finally may prove to be the most clinically practical method of detection.

The sensitivity of PAT to detect small embedded tumours, differentiate objects in layered tissues such as the skin and image blood vessels with high resolution has been reported by several groups [24, 30-39]. In recent years, many different methods have

been developed to generate PA images. For example, focused ultrasonic transducers have been used to localize the PA sources in linear or sector scans and then reconstruct the images directly from the data, analogous to clinical ultrasound [40]. Another method which is more commonly employed is the use of wideband unfocused detectors to detect the PA pressure transients and reconstruct the image by scanning the acoustics waves generated due to the absorption distribution within the sample. This reconstruction is an inverse source problem and many methods can be used including the weighted delay-and-sum, optimal statistical Radon transform and the back-projection method based on the Fourier transform [33, 41-44].

As early as 1995, *Kruger et al.* demonstrated how to obtain two dimensional images in tissue-mimicking phantoms using the Radon transform [45]. Soon after they showed that it was possible to differentiate among different types of tissues in porcine kidney with PAT [46] and detect early cancers in the human breast tissue using PAT [46, 47]. The imaging of deeply embedded tumours, such as breast tumours, was also followed up by *Esenaliev et al.* [48], *Manohar et al.* [36],*Oraevsky et al.* [48, 49] and *Andreev et al.* [10] who used an arc-array of PVDF transducers to image deeply embedded tumours in human breast tissue. Kolkman *et al* [50] used photoacoustic imaging to detect and resolve blood vessels while *Paltauf et al.* [37] used an imaging camera and a HeNe photoacoustic wave detector to get two dimensional images of small absorbers such as hair and small absorbing spheres. PA image contrast caused by heat-induced changes as a result of tissue coagulation during thermal therapy due to changes in optical absorption and thermo-elastic properties of tissues have been reported by *Spirou et al.* [51] and *Richter et al.* [52]. A different method of detection using a Fabry Perot interferometer system has

been used by *Beard et al.* to detect displacement on the surface of a sample induced by PA signal by observing optical interference patterns [32, 53, 54]. This technique has potential where backward-mode detection is the only option.

1.7 Photoacoustic Tomography in Thermal Therapy

Minimally invasive thermal therapy (MITT) has been explored as a means of treating small solid tumours with minimal damage to adjacent soft tissue by achieving coagulative necrosis in a targeted tumour region over a period of a few minutes. Coagulation occurs between 55°C and 95°C and can be characterized by a change in the tissue optical and mechanical properties [55] as seen in Figure 1-5. Laser MITT was introduced by Bown [56] and has been investigated by researchers as an alternative treatment modality for many tumours including the breast [57], liver [58] and prostate [59].

The damage to tissue is a function of both temperature and exposure time. Thermal damage is quantified by the thermal dose and is defined as the time at which tissue should be maintained at 43°C for an equivalent therapeutic effect to occur. It can be calculated from the time-temperature history using [60]:

$$t_{43} = \int_{t_{initial}}^{t_{final}} C^{(43-T)} dt \tag{1.10}$$

where t_{43} is the equivalent time at 43°C and T is the history of the time-temperature between $t_{initial}$ and t_{final} and

$$C = \begin{cases} 0.25 & for\ T < 43^{\circ}C \\ 0.5 & for\ T \geq 43^{\circ}C \end{cases} \tag{1.11}$$

The greatest challenge in TT is the capability to target a specific tumour without thermally damaging the surrounding healthy tissue. Due to the dynamic changes in temperature, optical and mechanical properties during TT, the ability to model and predict the treatment affects is very complicated. Since there is a large variability in the type of response among patients, a solution to minimize risk and account for dynamic changes is to monitor and implement a feedback control system into the treatment protocol. Various minimally or non-invasive methods of guiding and monitoring MITT include fluoroptic temperature sensors [61], magnetic resonance temperature imaging (MRTI) [62-64], the use of radiance/fluence probes [65, 66] and ultrasound imaging [67].

Models have been used to predict tissue damage but are limited as they cannot account for the large dynamic ranges of tissue optical properties during the heating process. Therefore, monitoring MITT is mostly conducted by means of probes placed within the tumour volume. There are limitations to this practice, as probes are can only detect local changes in temperature and also generate artifacts due to direct absorption of NIR light. These phenomena can limit the accuracy of computing the tumour response due to incorrect temperature readings [61, 68]. MRTI has been demonstrated as another monitoring system to monitor prostate thermal therapy, however it is costly thus limiting its use [62, 64].

There are several benefits in using PAT as a guiding and monitoring system in TT. It has the potential to accurately discriminate a tumour from the surrounding normal tissue and then provide an effective means of real-time mapping of treatment progression

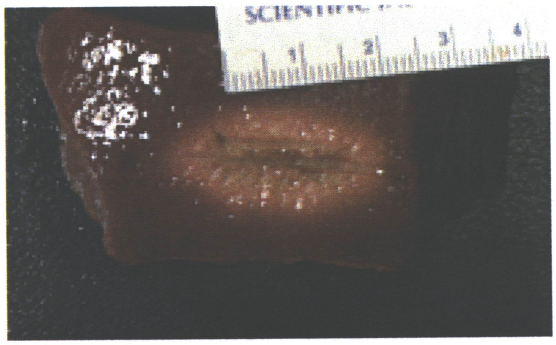

Figure 1-5: Lesion caused in bovine liver using 4W CW laser for 10 minutes at 805nm with a 2 cm cylindrical diffuser tip

during TT since the changes in the tumour optical and mechanical properties can be identified. This will ensure the least amount of healthy tissue damage while targeting the tumour volume. PAT has an advantage over pure optical techniques due to its hybrid nature as it can detect both optical and mechanical changes in the tissue thereby compensating for the dynamic changes that can occur during TT.

1.8 Outline

Chapter 2 will discuss the implementation of a working prototype PA system and detail how to generate, detect and reconstruct a PA image. In Chapter 3, monitoring of TT will be explored, in particular, a characterization of how TT affects a PA signal due to the changes in both optical and mechanical properties that occur during tissue coagulation. The final chapter will present the conclusions and future work.

Aims

1. Develop and build a working PA prototype system. Technical specifications and a detailed description of how the system is implemented and operated are detailed in Chapter 2.
2. Measure optical properties of turbid tissue-like media using a double integrating sphere (DIS) system.
3. Produce phantoms with different optical and mechanical properties that mimic the optical and mechanical properties of tissue. Two different phantoms are used: (i) gelatin phantoms – that mimic the optical properties of native and coagulated tissue and (ii) albumen phantoms that mimic both the optical and mechanical properties of prostate tissue in its native and coagulated states.
4. Demonstrate the effectiveness of PAT and evaluate the ability of detecting thermal lesions using tissue mimicking phantoms.
5. Image thermal lesions in bovine muscle and bovine liver and demonstrate the effectiveness of using PAT to detect and image lesions in tissue *ex vivo*.
6. Demonstrate selective imaging using PAT. Illustrate how image contrast can be influenced in PAT by matching the illuminating wavelength with the optical properties of a sample.
7. Demonstrate the real time capability in monitoring and detecting thermal lesions using PA. The PA signals are influenced by the optical and mechanical changes in tissue during thermal therapy. By understanding how the changes affect the PA signal, the potential for real time monitoring of thermal therapy is possible.

2 MATERIALS AND METHODS

2.1 Introduction

By combining the benefits of conventional optical and ultrasound imaging, PA imaging inherently possesses good optical contrast and high spatial resolution. This is possible due to the heterogeneity of optical absorption within tissues thereby creating pressure transients which effectively convert the optical information into sound. This information is far less susceptible to acoustic attenuation and absorption and can travel further with little loss of signal integrity in comparison to light, which is highly scattering and absorbed very quickly. Chapter 2 reviews the experimental setup of a working prototype single transducer PA system. It details the image reconstruction algorithm which creates a two dimensional image from the detected PA signals using a radial back-projection technique. Optical properties of tissues are measured using a setup called a double integrating sphere (DIS) system. Using a white light source, it calculates the absorption and scattering coefficient by measuring the amount of light that is reflected by and transmitted through a sample. Also, discussed is the preparation for two types of phantoms; the first is gelatin based where the optical properties of the target and the surrounding can be adjusted to mimic different optical properties of native and coagulated tissue. The other phantom is albumen based which not only aims to mimic the coagulative nature of prostate tissue when heated during TT, but also its optical properties.

2.2 Photoacoustic Tomography Experimental Setup

There are two main components to any PA system: one that generates EM radiation (eg. light) and the other that detects the acoustic waves generated by the PA effect. The experimental setup of PAT used in all experiments in this thesis is shown in Figure 2-1.

Laser light is delivered using a Vibrant B 532 (Opotek Inc., Carlsbad, CA, USA) laser system fed by a Q-switched Nd:YAG laser at 1064nm with a pulse duration of ~6.5ns and a repetition rate of 10Hz. The maximum output power of the Nd:YAG laser is 800mJ/pulse with a beam diameter of ~9mm. This source is fed into an Optical Parametric Oscillator (OPO) which provides many wavelengths that are tunable between 680nm – 950nm delivering a maximum power output of 75mJ/pulse at ~710nm. The output of the OPO is the irradiation source. Due to the Gaussian nature of the laser beam, an optical engineered diffuser (RPC Photonics, Rochester, NY, USA) is used to homogenize the beam to provide a uniform fluence field before illuminating the sample from the top. The engineered diffuser also diverges the beam so that the entire top surface of the sample is properly illuminated. The pulse energy density on the sample surface is limited by the MPE for human skin at a specific wavelength as defined by ANSI (Section 1.4).

The PA system, designed in-house, consisted of one detection channel which can receive PA signals. A variety of ultrasonic transducers can be used to detect objects, however, in this work, a transducer having a central frequency of 1MHz (Panametrics–NDT V-303, Waltham, MA, USA), with an active surface diameter of 10mm, is sufficient

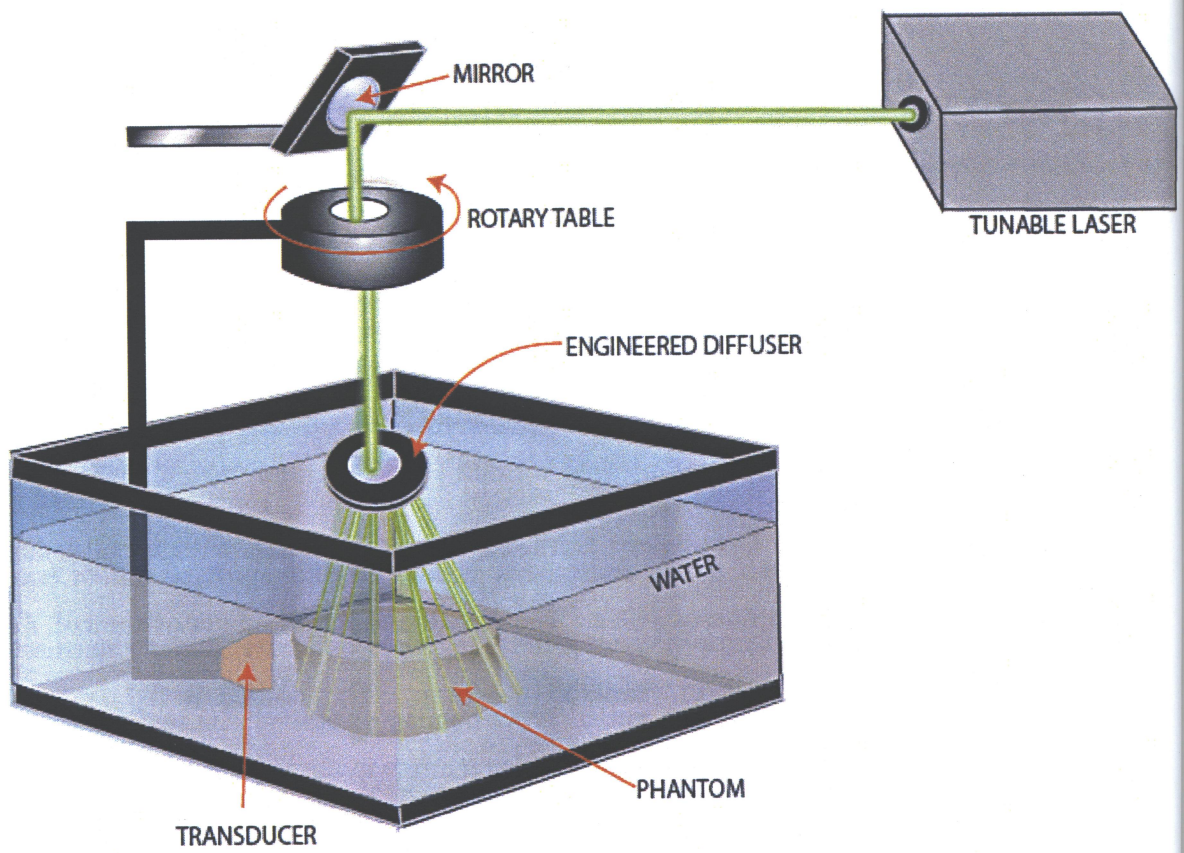

Figure 2-1: Photoacoustic Tomography Experimental Setup

and therefore used. The nominal bandwidth of the transducer is approximately 60% of the central frequency. The transducer converts the laser-induced photoacoustic waves into electrical signals that are amplified by a low noise power amplifier (Panametrics-NDT 5670, Waltham, MA, USA).

The transducer is mounted to a post and positioned so that it can rotate in a complete 360° circular scan in a horizontal plane around the sample. It is also vertically adjustable to scan a particular plane of interest. The post is connected to a motor driven rotary table which can sequentially move with a variable step size (typically between 1° – 3°) in a circular manner. A stepper motor (Parker Hannifin Corp.) drives the rotary table which is controlled by a LabView program. To ensure best detection, the active surface

of the transducer is aligned so that it is perpendicular to the rotational axis of the circular path by which the transducer face follows. For optimal coupling, the transducer and the sample are immersed in water and the SNR of the signals is improved by averaging over several acquisitions at a particular transducer location. For random Gaussian noise, the improvement in SNR is proportional to square root of the number of averages i.e. if 36 measurements are averaged the SNR is improved by a factor of $\sqrt{36} = 6$ times. To prevent aliasing, a low pass filter connected at the input of an oscilloscope filters frequencies greater than half the sampling rate.

An oscilloscope card (National Instruments NI-5112) digitizes the photoacoustic signal. It is controlled by LabView which synchronizes the acquisition from the trigger generated when the laser fires and then automates the data acquisition and positioning of the transducer. Figure 2-2 shows the sequential process in which signals are acquired. First, the stepper motor is energized and driven to a predetermined location. Once the transducer is positioned, the data acquisition card captures the signal which is synchronized with the trigger of the laser pulse. SNR is improved by averaging between 30 – 50 times and then the digitized signal is written to file for later retrieval. This completes one step of the process and the transducer is then moved to the next location until an entire 360° scan is completed.

A digital band-pass filter corresponding to the central frequencies and bandwidths of the ultrasonic transducers is used to eliminate additional noise from the signals. Finally, an image is reconstructed using a radial back-projection (RBP) algorithm by mapping the absorption of light using the information contained within the acoustic waves that were detected and stored from all the different transducer locations.

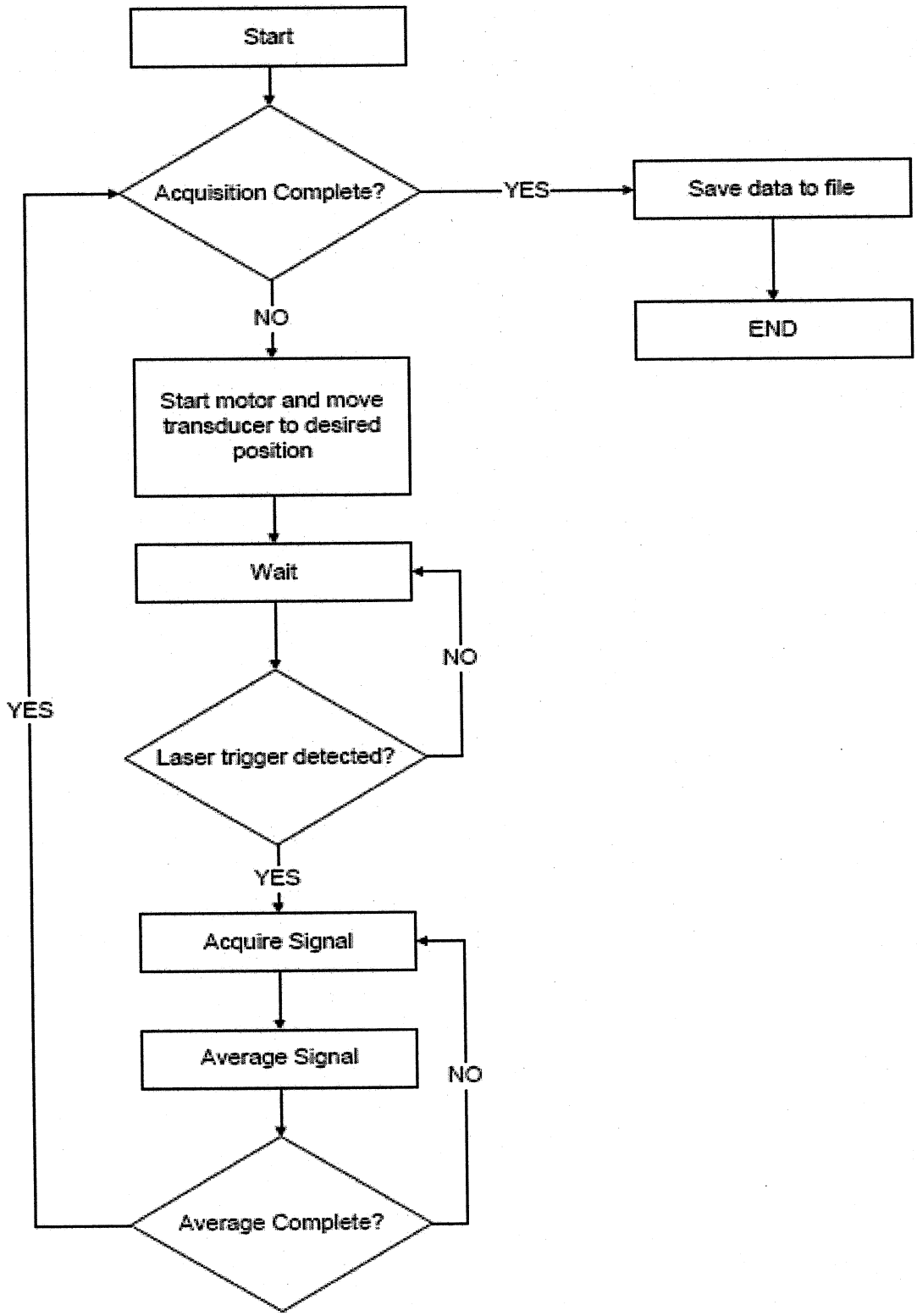

Figure 2-2: Single transducer data acquisition flowchart

2.3 Photoacoustic Image Reconstruction

A RBP algorithm is used to reconstruct and create a visual two dimensional image from PA signal data. It relies on signal integrals projected backwards onto a grid while taking into account the angle of acceptance of the transducer at each successive location during the scan. The image represents the distribution of the product of thermoacoustic efficiency, optical absorption coefficient, and effective laser fluence in the sample [3].

In response to a heat source, the behavior of photoacoustic waves with pressure $p(\mathbf{r},t)$ at position $\mathbf{r}$ at time t in an acoustically homogenous liquid like medium can be expressed as [69]:

$$\frac{\partial^2 p(\mathbf{r},t)}{\partial t^2} - c^2\nabla^2 p(\mathbf{r},t) = \frac{c^2\beta}{C_P}\frac{\partial H(\mathbf{r},t)}{\partial t} \tag{2.1}$$

$H(\mathbf{r}, t)$ is the heat-producing radiation deposited in the tissue per unit volume per unit time which can be expressed by:

$$H(\mathbf{r},t) = A(\mathbf{r})I(t) \tag{2.2}$$

where $A(\mathbf{r})$ describes the optical energy deposition within the tissues and $I(t)$ describes the temporal shape of the irradiation pulse, which can be further expressed as a delta function, $\delta(t)$, for impulse heating.

The objective of PAT is to reconstruct the distribution of the optical absorption $A(\mathbf{r})$ in tissue from a set of detected acoustic signals $p(\mathbf{r}, t)$. For the case where the scanning radius is in a circular scan configuration, the exact inverse solution can be derived, however, it is computationally intensive. A simplified version of the image reconstruction algorithm can be used if the detection radius, r_0, is assumed to be much larger than the wavelength that corresponds to the central frequency of the detection device i.e. far-field detection [39]. This assumption holds true in this case and thus significantly reduces reconstruction time. The approximated inverse solution is [39]:

$$A(r) = -\frac{r_0^2 C_P}{2\pi c^4 \beta} \int_{\theta_0} d\theta_0 \frac{1}{t} \frac{\partial p(\mathbf{r}_0, t)}{\partial t}\bigg|_{t=\frac{|\mathbf{r}_0 - \mathbf{r}|}{c}} \tag{2.3}$$

where $p(r_0, t)$ is the photoacoustic signal detected at each scanning angle θ_0. The relation of $p(r_0, t)$ from r with respect to the origin, O, is depicted in Figure 2-3. RBP images using a limited number of transducer positions will inherently produce artifacts in the reconstruction due to an incomplete data set. To minimize artifacts techniques such as signal interpolation can be used. Also, image quality can be improved by using image processing after reconstruction. To attain visually satisfactory images the step sizes in the experiments are limited between 1° – 3° over the 360° circular scan.

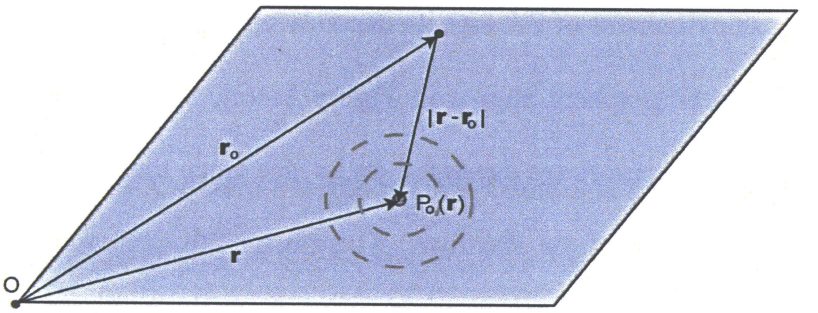

Figure 2-3: Geometry of PA detection used in RBP

2.4 Resolution and Image Analysis

Resolution in PAT is limited by the laser pulse duration and the bandwidth of the transducer. Although Equation (2.3) can exactly reconstruct the varying absorption contrast in tissue, it assumes an ideal acoustic detector that is able to cover the entire frequency spectrum. In practice, however, for a single transducer element, this is impossible and so only a fraction of the spectrum is detected thereby acting as a band-pass detector. The signals attained by limited bandwidth transducers cause blurring in the reconstructed image. Blurring is further increased by the duration of the laser pulse since Equation (2.3) also assumes impulse heating. Therefore, the reconstructed image is influenced by a convolution between the differences in absorption of tissue structures, the pulse width of the laser profile and the impulse response of the acoustic transducer. The reconstructed image *I(r)* can be described by [70]:

$$I(r) = S(r) * L(t \cdot c) * D(t \cdot c) \tag{2.4}$$

where $S(r)$ represents the optical structure of tissues, $L(t \cdot c)$ and $D(t \cdot c)$ are the laser pulse and transducer impulse responses in the spatial domain, respectively.

The frequency content of PA signals depends on the size of the absorbers. In the example of an absorbing sphere shown in Figure 1-4(c), an N-shaped profile will be observed and its characteristics are depended on its size since the opposite polarity peaks correspond to the diameter of the absorber. Therefore, with decreasing diameter of the absorbing sphere, an increase in PA signal frequency will be observed. This shows the importance of choosing the optimal transducer with the best frequency response for a specific application. Figure 2-4 shows the dominant frequency from spherical PA signals as a function of diameter [71]. It shows that by using high frequency transducers (band-limiting to only high frequencies), edges or boundaries of absorbers will be detected since there is a sharp difference at boundaries. The internal contents, however, have small variation in optical properties and this information will be lost because high frequency transducers will not be able to properly detect the slow changes associated with the smooth variation in optical properties within the object. Therefore, the larger the frequency response of a transducer is, the better the ability to visualize the entire object.

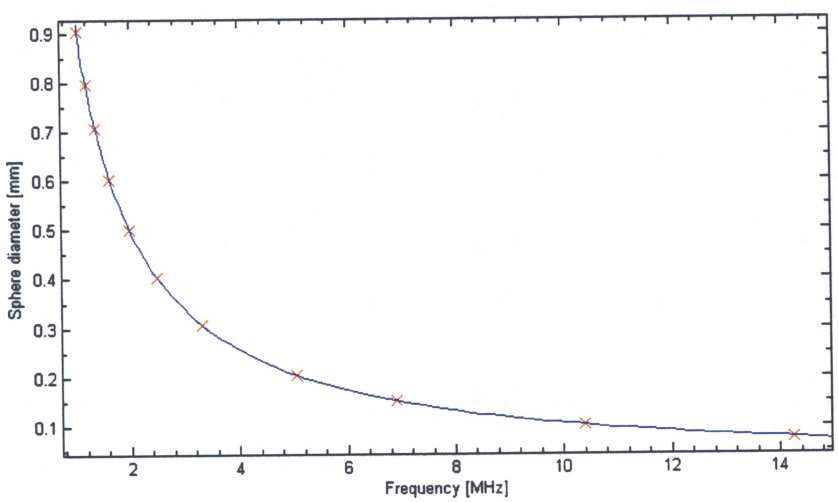

Figure 2-4: Dominant frequency of PA signal versus sphere diameter

2.5 System Verification

To calibrate the PA system a turbid gelatin phantom is constructed as explained in Section 2.7. One highly absorbing gelatin target with a circular cross section of diameter ~10mm is placed in the centre of a gelatin phantom which has a low optical absorption but is highly scattering as shown in Figure 2-5(a). The phantom has a diameter of 8cm and a height of 5cm and is illuminated with a wavelength of 810nm from above causing the light to be incident on the top face of the phantom. The acoustic pressure wave is detected in side mode using a 1MHz transducer in 2° steps around the phantom. Figure 2-5(b) shows the PA profile detected by the transducer when light is incident on it. Due to the symmetric nature of the target with respect to the detector, in this simple case, the PA profile should be similar at all transducer positions. The result is acoustic waves with profiles resembling depth or axial distribution of the absorbed optical energy. The N-shape feature is caused by the absorbing target with the distance between the peaks corresponding to the diameter of the target i.e. the time $t_N = d/c$, where d is the diameter and c is the speed of sound in the target. This experiment shows that the system responds and detects the PA wave as expected by the theoretical models.

2.6 Double-Integrating Sphere System

To understand and better predict light propagation and distribution within tissues, an accurate determination of the optical properties is needed. A double integrating sphere

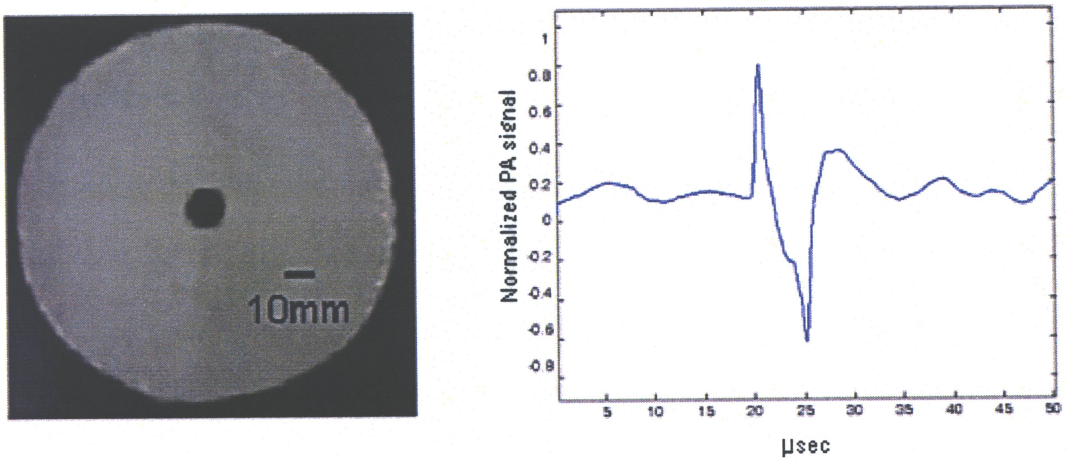

Figure 2-5: (a) Turbid gelatin phantom with highly absorbing target. (b) Corresponding normalized N-shaped PA signal

setup (DIS) is used to experimentally measure optical properties of tissue phantom samples. This is done by measuring the diffuse reflectance, R_d, diffuse transmittance, T_d, and the collimated transmittance, T_c, of an irradiated slab of tissue between the two spheres that collect light. From these three measurements the optical properties of tissues can be estimated.

To measure the optical properties, a sample is placed between two identical integrating spheres of 30.5 cm (12 in.) diameter with a circular sample window of 25mm diameter and illuminated with a white light (Ocean Optics, Dunedin, FL, USA) operating at 7 W. Light is focused onto the sample using a set of optics that collimate and produce a 5 mm beam diameter. R_d and T_d are collected in the first and second sphere respectively and T_c is collected by capturing the collimated transmittance at a distance of 100 mm beyond the second sphere as shown in Figure 2-6. Measurements are collected using an optical spectrometer which is capable of detecting light from 650nm – 900nm. R_d and T_d are measured relative to a baseline signal using a 99% reflecting plate (Sphere

Optics, SG2052, Concord, NH, USA) that is placed at the sample aperture while T_c is determined

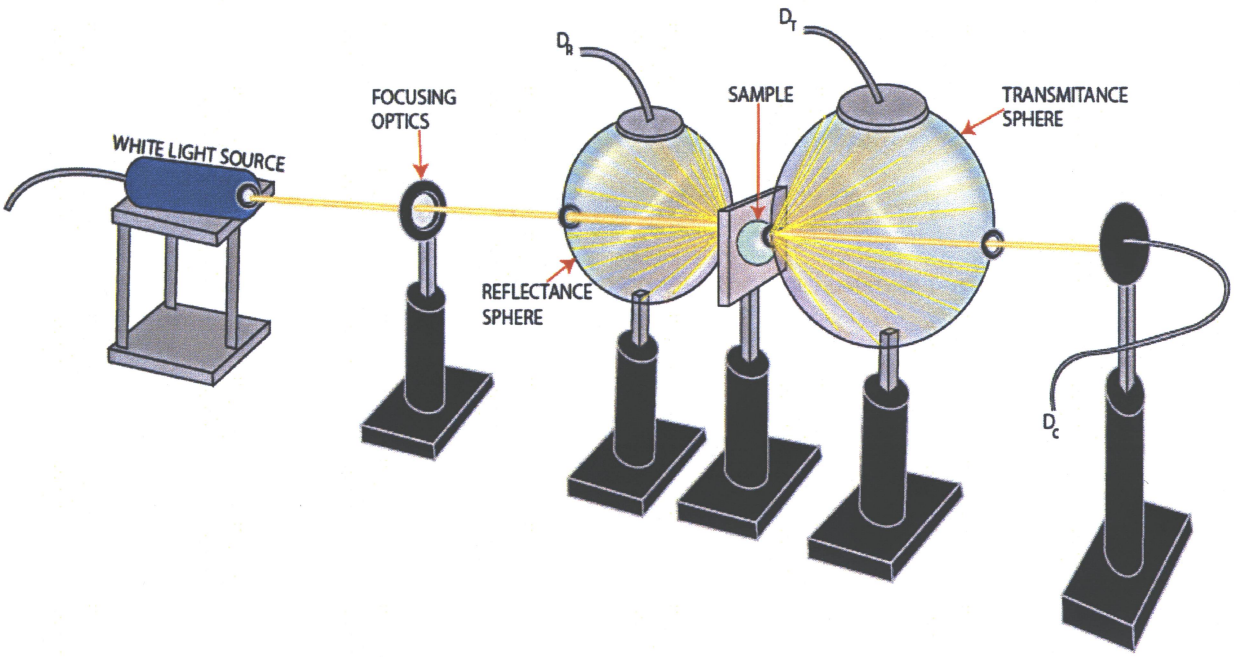

Figure 2-6: DIS experimental setup using white light source. D_R, D_T, D_C are the locations where R_d, T_d, and T_c are measured from respectively.

relative to 100% transmission i.e. with no sample.

From these three measured parameters, it is assumed that a unique relationship exists from which the absorption coefficient and scattering coefficient can be derived. Different methods to compute the optical properties on measured values are available like the inverse adding doubling algorithm (IAD) [72]. Another more sophisticated but highly computationally intensive method is using Monte Carlo (MC) simulations where the measured values are correlated using an inverse MC [73, 74].

2.7 Tissue Mimicking Gelatin Phantom

The use of tissue samples can sometimes be impractical due to the constraints of accessibility and storage. Reproducibility of results may also be poor because of the difficulty in finding identical specimens due to the complex structures that exist within the tissue such as the vasculature. An alternative method is to use tissue-mimicking phantoms which are usually homogeneous and provide a means of producing highly repeatable samples for investigating the propagation and absorption of light. Phantoms do not reflect the true complexity of tissue structures making their response an approximation however, they provide a means of testing the parameters and assumptions made in mathematical models and may indicate generally important tissue features for PAT [75].

Tissue mimicking phantoms are made of Type A Gelatin from porcine skin (300 Bloom, Sigma) and distilled water. One litre of distilled water is brought to a boil and then 85g of Type A gelatin is added and allowed to dissolve. To mimic the effect of scattering, 10ml/L of homogenized whole milk (3.25% fat content) is added. The entire solution is stirred until it is homogeneous and then the mixture is poured into a mold where small targets are added by suspending them using thin wires. The entire mold is placed into the fridge to cool for approximately 4 hours. Figure 2-7 shows gelatin phantoms with different optical properties. The phantom on the left is plain gelatin - having low absorption and scattering therefore appearing transparent. The middle phantom has a high scattering component due to milk causing the whitish appearance. The last phantom to the right is highly absorbing caused by the addition of India Ink.

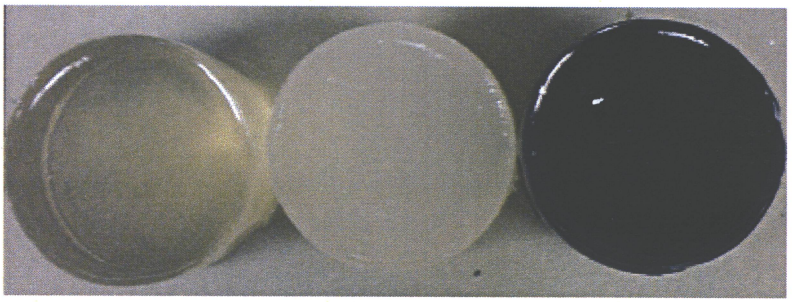

Figure 2-7: Examples of gelatin phantoms – the left phantom is pure gelatin, the middle contains milk causing high scattering and the right phantom contains a high concentration of India Ink making it highly absorbing.

Published values are reported which can be used to estimate the optical properties of gelatin. The values as determined by *Spirou et al* for the optical absorption and scattering are ~0.13cm^{-1} and 4.2cm^{-1} respectively at 1064nm [51]. The main goal of using phantoms is to substitute them in the place of tissue and image embedded targets to serve as tumours with comparable optical properties. The targets are produced by taking a batch of the same gelatin solution and adding dye (India Ink) of different concentrations. They are then molded into many different shapes and placed within the phantom.

2.8 Tissue Equivalent Albumen Phantom

An albumen-based phantom is used for all TT experiments due to its ability to mimic tissue coagulation and its construction is based on a paper reported by *Iizuka et al* [75, 76]. Albumen is chosen because it is homogeneous, uniform in appearance and it is hypothesized that changes in optical and mechanical properties due to thermal denaturation is similar to that seen in tissue. It is comprised mainly of water (88.1%), globular proteins (10.2%) and lipids (0.05%) and is commercially available in powered

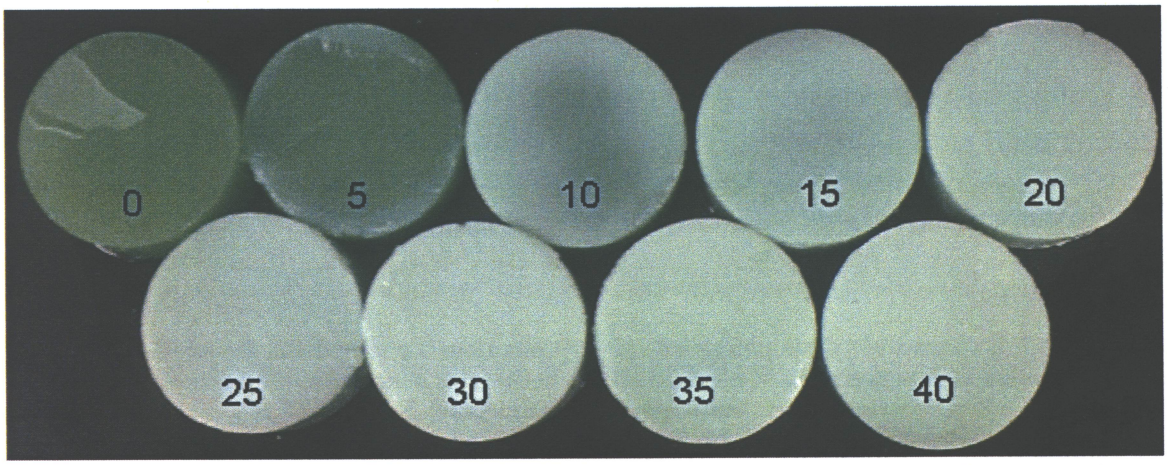

Figure 2-8: Albumen phantoms heated for different time periods. The number on each phantom represents the amount of time, in minutes, that each phantom was immersed in the water bath at 70°C

form, composed of dehydrated egg white. Exposure to heat causes an unfolding of the albumen proteins which produces the visible whitening and is quantified by an increase in the reduced scattering coefficient, similar to the response of tissue [77].

The phantom consists of chicken egg albumen (Crude, Grade II, Sigma, St. Louis, MO, USA), bacteriological agar (Agar #1, Oxoid, Hampshire, England) and Naphthol Green dye (Sigma, St. Louis, MO, USA) and is prepared by combining two mixtures: a stock albumen solution and an agar-dye solution. Stock solution of the albumen mixture consists of 77.8% by weight distilled water and 22.2% by weight powdered egg white. The albumen is stirred until fully dissolved producing a translucent yellow liquid. A 53.3% by weight albumen stock solution is measured and warmed up in a water bath to 40°C to be mixed with the agar-dye solution later. The dye solution is prepared separately by dissolving 0.387g of Naphthol Green dye powder into 1 liter of distilled water. A 13.3% by weight dye solution is then combined with a 32.0% by weight amount of distilled water. It is heated up to 70°C before adding agar powder of 1.4% by weight.

	μ_a [cm^{-1}]	μ_s' [cm^{-1}]
Native	0.50	2.67
Coagulated	0.7	13.1

(a)

	μ_a [cm^{-1}]	μ_s' [cm^{-1}]
Native	0.6	1.28
Coagulated	0.94	13.0

(b)

Table 2-1: (a) Optical properties of albumen phantoms in native and coagulated states as reported by *Iizuka et al* and (b) optical properties of albumen phantoms using the same recipe and measured using the DIS system.

The agar-dye solution is slowly heated to 85°C and then cooled down to 45°C. At this temperature, the agar-dye solution is mixed into the albumen stock solution, poured into cylindrical molds with diameter of 5cm and height of 3cm and cooled to room temperature – typically around 2 hours.

Figure 2-8 shows different phantoms that have been heated in a water bath at 70°C in five minute intervals from five minutes to forty minutes to demonstrate how the optical properties change when exposed to heat. The optical properties of these phantoms as reported by *Iizuka et al* at 850nm are listed in Table 2-1(a) while the optical properties measured by the DIS system at 850nm is shown in Table 2-1(b) [75]. The phantoms used to represent the native and coagulated states of prostate tissue when measured with the DIS system are phantom 0 and phantom 40 respectively from Figure 2-8.

2.9 Summary

This chapter outlined the implementation of a working prototype PA system and fabrication of tissue mimicking phantoms. Being able to characterize optical properties of samples makes it possible to study the response generated by the PA effect. This is done by capturing acoustic signals at several angles around a sample and from this a two

dimensional image is reconstructed that shows the heterogeneity of optical absorption in the sample. The use of phantoms allows for a more controllable and repeatable experimental response thereby reducing the large variations mostly observed in tissue – making it easier and more practical to understand how PA signals are affected by different physical conditions.

3 PHOTOACOUSTICS IN MONITORING THERMAL THERAPY

3.1 Introduction

The goal of this work is to investigate the possibility of using PAT to image tissue during TT and also to monitor tissue coagulation induced by TT in real time by analysis of the associated PA signals.

TT is the treatment of cancerous tissue by causing coagulative necrosis due to exposure to temperatures in excess of 55°C. Experimentally, it has been known that when coagulation occurs, not only does the mechanical structure of tissue change but also the optical properties [51, 52, 75]. This change should affect the PA signals detected making it easier to differentiate them from the surrounding healthy tissue. One of the current clinical limitations of TT is the inability to monitor the treatment in real-time. PA is sensitive to changes in both the optical and mechanical properties of tissue and therefore is a potential candidate for the monitoring of TT.

To demonstrate the ability to image native and coagulated tissue using PAT, tissue mimicking gelatin phantoms are made having optical properties similar to native and coagulated prostate tissue as reported in literature [78]. Targets are embedded in a gelatin phantom. The optical absorption and reduced optical scattering of the targets are $\sim 0.6 cm^{-1} - \sim 1.6 cm^{-1}$ and $\sim 6 cm^{-1} - \sim 17 cm^{-1}$ respectively, similar to optical properties of

coagulated tissue. In addition, thermal lesions created in bovine muscle and bovine liver are imaged.

Selective imaging using PAT is also demonstrated by embedding two targets into a turbid gelatin phantom with each target containing a different dye i.e. different absorption coefficient. By illuminating with several different wavelengths between 730nm and 950nm, the contrast of the imaged targets varies depending on its wavelength specific absorption coefficients.

To demonstrate the capability of PA to monitor TT, albumen phantoms that mimic both the optical and mechanical properties of prostate tissue are developed. By heating phantoms for different time periods, a correlation between the thermal dose and the PA signals detected can be investigated. With increased thermal dose a measurable change in the PA signal relative to a native sample is anticipated. This information potentially can be used to monitor the coagulation of tissue during TT.

3.2 Photoacoustic Images of Gelatin Phantoms

Four phantoms, as explained in Section 2.7, are constructed with different targets of varying optical properties, shapes and sizes as shown in Figure 3-1(a – d) and imaged to demonstrate the capability of PAT in imaging localized changes in tissue properties. The physical properties of all the different targets shown are listed in Table 3-1. The optical properties for the targets are measured using the DIS system. The choice of size and optical properties are made to mimic tissues. For all experiments discussed in Section 3.2 the illumination is at 810nm and the fluence field is set below 5mJ/cm^2 (well below

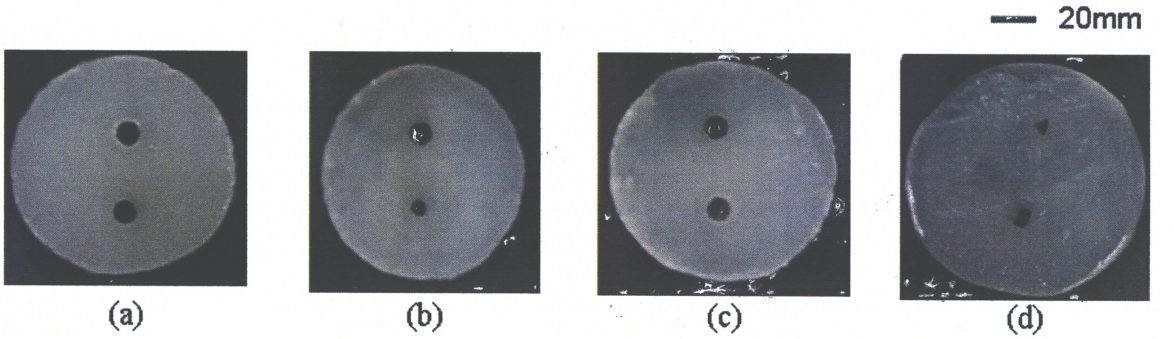

Figure 3-1: Turbid gelatin phantoms constructed with different targets varying in size, shape and optical absorption.

ANSI standards). If two absorbers are positioned on one axis in the phantom as in Figure 3-1(a), the spatial distribution can be calculated. Figure 3-2(a) shows one such RF signal recorded from the two targets spaced 1cm from the centre with the transducer positioned perpendicular to the bottom of the lower target shown in Figure 3-1. This demonstrates the potential to use PAT for localization and size estimation. When the transducer is positioned to the right of the targets equidistant from each of them as seen in Figure 3-2(b), the signal detected is a superposition of the PA profiles from both targets.

Figure 3-3 shows a reconstructed image of a phantom which contains two cylindrical targets with different radii but identical optical absorption of ~1.6cm^{-1} corresponding to the photograph in Figure 3-1(b). Since both targets have the same absorption characteristics, they have similar signal amplitudes and therefore have comparable pixel intensity values. The difference in cross sectional diameters is visually recognizable from the reconstructed image and can be calculated from the difference between the peak-to-peak times (t_N) from the N-shaped profiles. The first N-shaped signal corresponds to the bottom target while the second N-shaped signal results from the top target. $\Delta 1$ and $\Delta 2$ in Figure 3-3(b) are 2.8μsec and 4.8μsec, respectively. Assuming

	Position	Dimensions (± 0.5mm)	μ_a [cm^{-1}] (± 0.2cm^{-1})
Figure 3-1 A	Top	7mm diameter	1.6
	Bottom	7mm diameter	1.6
Figure 3-1 B	Top	7mm diameter	1.6
	Bottom	4mm diameter	1.6
Figure 3-1 C	Top	7mm diameter	1.6
	Bottom	7mm diameter	0.7
Figure 3-1 D	Top	4mm base, 5mm height	1.6
	Bottom	6mm x 3mm	1.6

Table 3-1: Physical properties for all targets in Figure 3-1

the speed of sound in water to be 1500m/s, the cross-sectional diameter of the targets can be estimated to be 4mm and 6.75mm for the top and bottom targets, respectively. This correlates well with its physical dimensions listed in Table 3-1.

Figure 3-4(a) shows two spherical targets with different optical absorption coefficients embedded in the gelatin phantom. The photograph of this phantom is shown in Figure 3-1(c). The upper target has a μ_a of ~1.6cm^{-1} while the lower target has a μa of ~0.7cm^{-1}. The optical absorption of the bottom target is lower and hence, a weaker PA

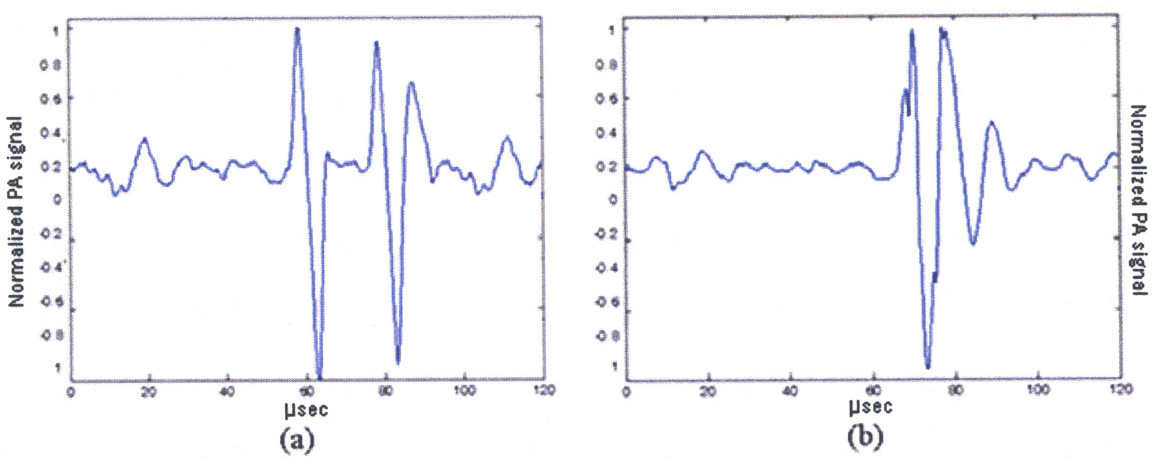

Figure 3-2: Normalized PA signals captured from two different transducer locations from a phantom with two absorbing target as shown in Figure 3-1(a). (a) transducer positioned directly below lower target and (b) transducer positioned to the right of the phantoms equidistant from both targets.

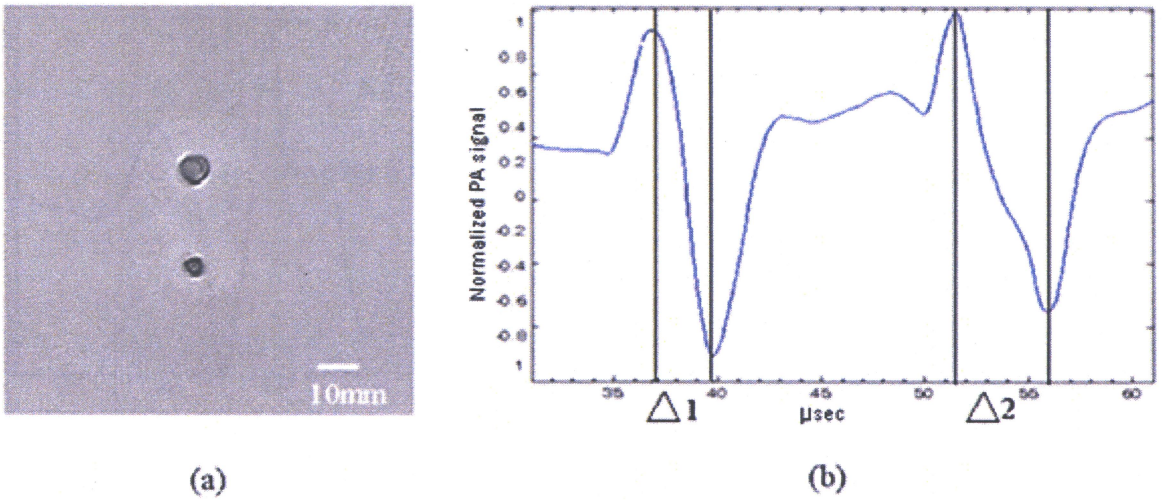

Figure 3-3: (a) PA image of phantom containing two targets with different radii shown in Figure 3-1(b). (b) PA signal with transducer positioned directly below lower target. Diameter of each target can be determined from the signal data by calculating the difference in the time at which the signal peaks. The difference in peaks denoted by Δ1 and Δ2 are ~2.8 μsec and ~4.8 μsec respectively.

response is detected (Figure 3-4(b)). The upper target, on the other hand, absorbs more light and in turn produces a stronger signal. The stronger signal translates into darker pixels in the reconstructed image thereby producing greater image contrast than the lower target. Δ3 and Δ4 in the graph correspond to 0.4 and 0.8 normalized units (normalized to the peak amplitude) respectively. This doubling of the PA signal agrees well with the increase in optical absorption as expected (Equation (1.7)), demonstrating a powerful advantage in PAT where contrast is produced by the inherent optical properties of a tissue target.

Figure 3-5 shows two absorbing targets in the shape of a square and triangle. The optical absorption of both targets is ~1.6cm^{-1} and they are easily distinguishable with clear edges. The photograph of this phantom is shown in Figure 3-1(d). This demonstrates the capability of the PA system to image arbitrary shapes.

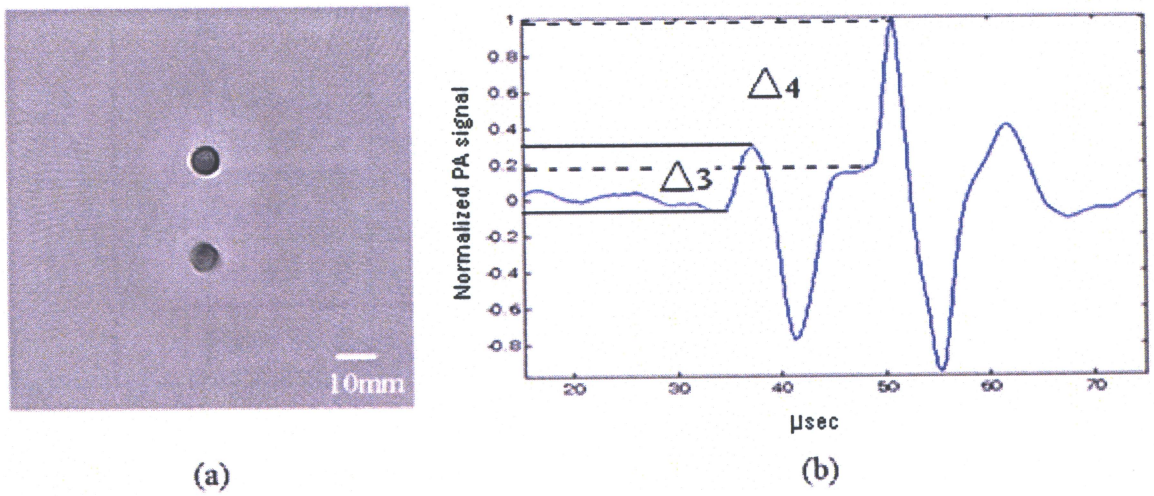

Figure 3-4: (a) PA image of phantom containing two targets with different optical absorptions with ~1.6cm^{-1} for the upper target and ~0.7cm^{-1} for the lower target photographed in Figure 3-1(c). (b) PA signal data showing the change in the rising peak due to the difference in optical absorption. The difference in the rising peak of each signal in normalized units denoted by Δ3 and Δ4 are ~0.4 and ~0.8 respectively. Higher optical absorption in a target will cause its PA signal to increase as seen above and create greater image contrast in the image.

In all the PA images, an optical diffuser is used to homogenize the incident light field on the phantoms. However, this cannot guarantee a uniform fluence incident on the targets since the light distribution from the laser is Gaussian. Hence, the number of photons absorbed by the target/phantom will vary as a function of radial distance from to the center of the beam such that, even with identical optical absorption, one target may appear brighter than another. Since this variation is not accounted for in the reconstruction algorithm i.e. the fluence field is assumed to be homogeneous, a quantitative comparison of the images is not possible. The reconstruction algorithm assigns a pixel value to a range of summed signal points after back-projection. This pixel assignment effectively normalizes the summation of signal amplitudes for a give pixel location and then calculates its grayscale value depending on the peak summation. Therefore, for a quantitative analysis of target absorption, one must compare pixel data

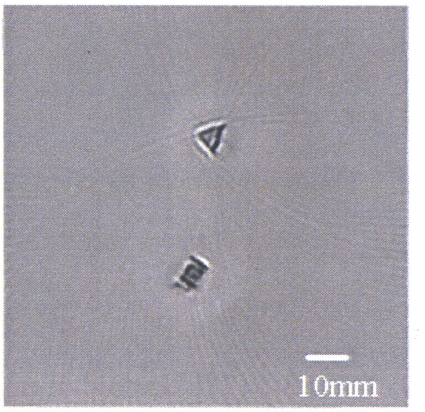

Figure 3-5: PA image of two absorbing targets in the shape of a square and triangle. Both targets have the same optical absorption.

from a single image since the grayscale assignment is processed using the same data set. Comparing multiple images will not necessarily yield a correct representation of the optical characteristics since the pixel values are proportionally allocated with reference to the peak within a specific image matrix. To compare multiple images, a reference target with known optical properties must be fabricated and imaged. By knowing the optical characteristics of the reference target and its PA response, it will be possible to scale the pixel values accordingly for identical exposure settings.

The above experiments demonstrate the potential of PAT to image small (< 5mm) diameter targets in a turbid gelatin medium using a 1MHz transducer. Due to the difference in optical properties between targets and the surrounding gelatin medium, the PA system is capable of discriminating with high image contrast.

	Wavelength	μ_a [cm^{-1}]	μ'_s [cm^{-1}]	μ_{eff} [cm^{-1}]
Human (native)	850nm	0.6	6	3.45
Human (coagulated)	850nm	0.7	13.8	5.52

Table 3-2: Optical properties of native and coagulated human prostate tissue [78]

3.3 Photoacoustic Images of Human Prostate Tissue Mimicking Gelatin Phantoms

To resemble native and coagulated prostate tissue, targets with optical properties similar to human prostate are constructed and imaged. The optical properties of human prostate at 850nm are shown in Table 3-2 [78]. Instead of embedding purely absorbing targets in a turbid gelatin surrounding, like previously done, in this experiment the embedded targets are constructed to mimic the optical properties of human prostate with both absorption and scattering components. Figure 3-6 shows the embedded targets in a clear gelatin phantom where the top target mimics coagulated tissue while the bottom target mimics native tissue.

The PA image, acquired at 850nm (Figure 3-7), clearly shows two targets and demonstrates the sensitivity of the system to image targets with optical absorption as low as $0.6cm^{-1}$. In the images, the darker pixels relate to greater PA signal strength. Although it is not visually apparent, in Figure 3-7(a), there is a difference in pixel intensity between the two

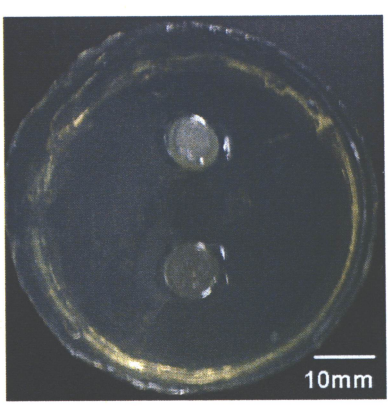

Figure 3-6: Optical mimicking phantom with two embedded targets representing the optical properties of native and coagulated prostate tissue as listed in Table 3-2. The lower target represents the native tissue while the upper target represents the coagulated tissue with μ_{eff} of 3.45 cm^{-1} and 5.52 cm^{-1} respectively.

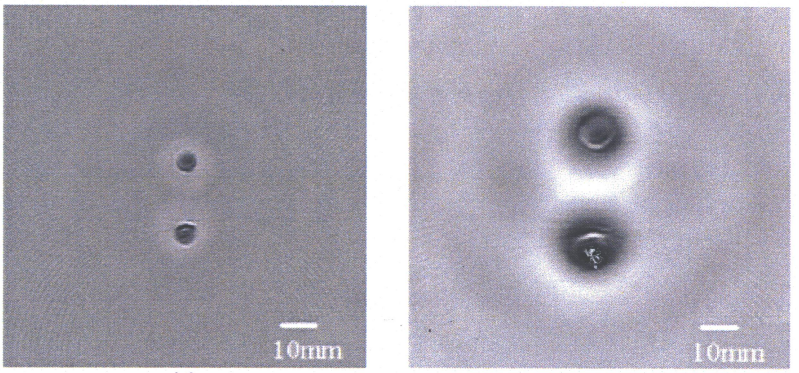

(a) (b)

Figure 3-7: Two different representations showing PA images of the gelatin phantom in Figure 3-6. The lower sphere represents the non-coagulated tissue while the upper sphere represents the coagulated tissue with μ_{eff} of 3.45 cm^{-1} and 5.52 cm^{-1} respectively.

targets. The averaged pixel value of the bottom target is 21% lower than the upper one. Although the optical absorption is higher in the upper target, the PA image does not show this. Instead, the lower target (with a lower μ_a) is 21% darker. The cause for not seeing a proportional increase in pixel intensity with optical absorption is due to the influence of optical scattering. Introducing scattering affects the propagation and penetration of light into the target and in turn, there is a reduction in PA signal strength. This reduction of the PA signal is shown as lighter pixels in the PA image. Another way of representing the image is by ignoring the derivative of the pressure in Equation (2.3) as shown in Figure 3-7(b). It produces an image with much lower resolution thereby causing the targets to appear larger than actual. Nevertheless, when depicted in this form, it is much easier to visualize which target produced a higher PA signal by examining the difference in pixel intensity.

When optical scattering is much greater than optical absorption (as in tissue), the propagation of photons within a target is limited and this affects the strength of the PA signal. As in this experiment, even though the optical absorption is slightly higher (Table 3-2) in the coagulated tissue mimicking target, the PA signal generated may not increase due to the

effects of scattering from within the target. Depending on where the sensing volume of the transducer is, the fluence within the target may be lower and thus overciming the effect if a higher μ_a.

3.4 Photoacoustic Images of Thermal Lesions in Tissue

After imaging gelatin phantoms using the PA system, which indicated the ability to detect absorbing targets, tissue experiments are performed. Two types of tissues are used (i) bovine muscle and (ii) bovine liver. A lesion is created in the tissue using a CW diode laser at 5W for 12 minutes until the centre of the sample reached a temperature of 75°C. The tissue sample is cooled to room temperature and then imaged.

Figure 3-9 is a PA image, illuminated at 950nm, showing a lateral cross section of the bovine muscle photographed in Figure 3-8. The laser fiber is embedded into the tissue sample which produces a well demarcated lesion inside the tissue sample. When dissected to

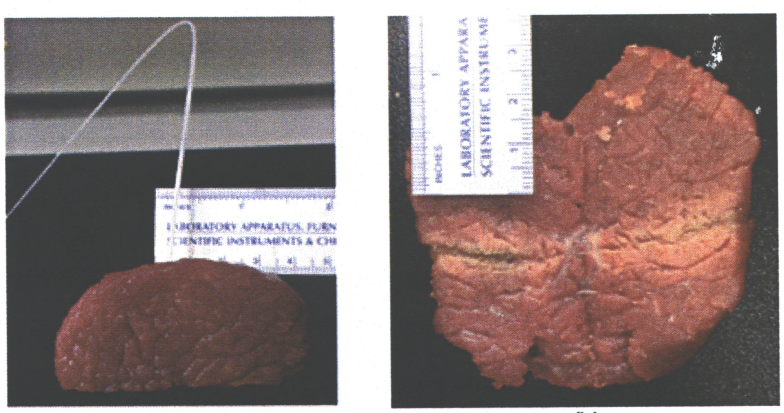

Figure 3-8: (a) Bovine muscle photographed from above showing inclusion where laser fiber is placed (b) bovine tissue transversal cross section showing extent of coagulation after laser heating.

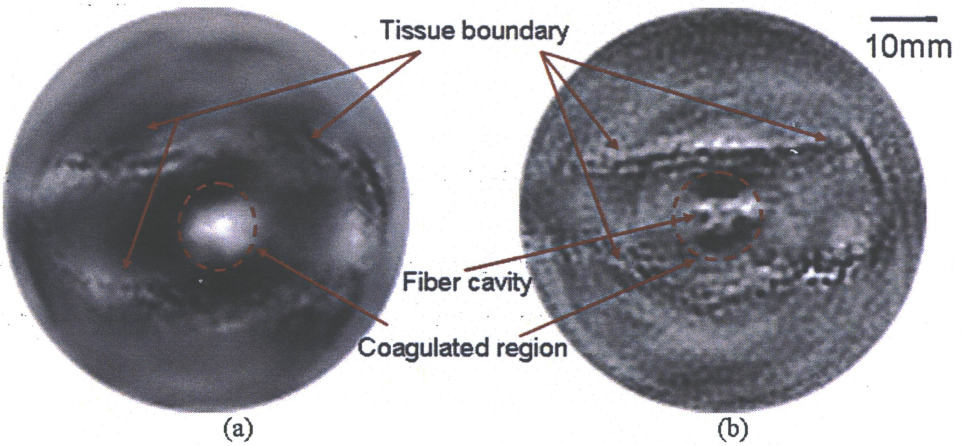

Figure 3-9: PA image of a bovine tissue sample imaged at 950nm as shown in Figure 3-8. The transducer is placed to detect a lateral cross section.

expose the middle of the sample, as shown in Figure 3-8(b), the extent of coagulation can be seen. The transducer (Figure 2-1) is positioned so that the active region detects signals in the lateral plane approximately 1cm below the top surface. Figure 3-9(a) ignores the derivative of the pressure when using the RBP algorithm. The coagulated region is depicted in white and is quickly recognizable. As the tissue coagulates, the optical and mechanical properties change causing whitening in the image [65, 79]. The dark pixels represent higher PA signal strength which is limited to the areas surrounding the lesion. Figure 3-9(b) is an image of the same sample using the RBP algorithm that has been pre-processed using digital signal processing techniques to filter noise and enhance edges in the image. The boundaries of the tissue sample are much more clearly observed with the coagulated region in the centre.

Figure 3-11 depicts a surface lesion in bovine liver imaged at 810nm. The fiber is placed on the top surface of the sample and held down with another larger liver sample to ensure that the fiber is in contact with the surface at all times and held in place. The liver is heated, using a CW 805nm laser set at 5W for 6 minutes, until the lesion surface reaches a temperature of 75°C and then cooled to room temperature. The photograph in Figure 3-10

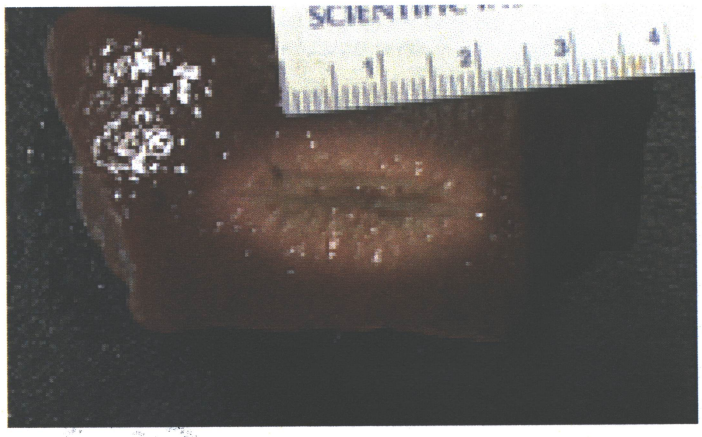

Figure 3-10: Bovine liver with surface lesion using CW laser at 5W at 805nm

shows the lesion created on the surface of the liver. Apart from the whitish coagulated region, two imprints are visually distinguishable – one from the fiber tip and the other from the temperature probe. The PA image in Figure 3-11(a) ignores the derivative of the pressure in the RBP algorithm. The image shows the extent of the lesion where the coagulated region is depicted in white. The areas surrounding the coagulated region in the photograph are the unaffected parts of the liver, and may absorb more light producing a darker pixel value. Figure 3-11(b) is pre-processed using digital signal processing techniques before image reconstruction producing an image with less noise and better resolution as done for the bovine muscle lesion in Figure 3-9(b). The boundaries are more pronounced and the fiber and temperature probe imprints in the coagulated region can be distinguished.

The signal pre-processing included several steps. A peak detection algorithm is used to identify the region of interest. Once the region of interest is found, other values outside this window are set to zero. This removes unwanted noise and also improves image contrast since the grayscale levels are discretized over a smaller range of values. Finally, signal filtering is performed to produce the best image. This included noise reduction using a

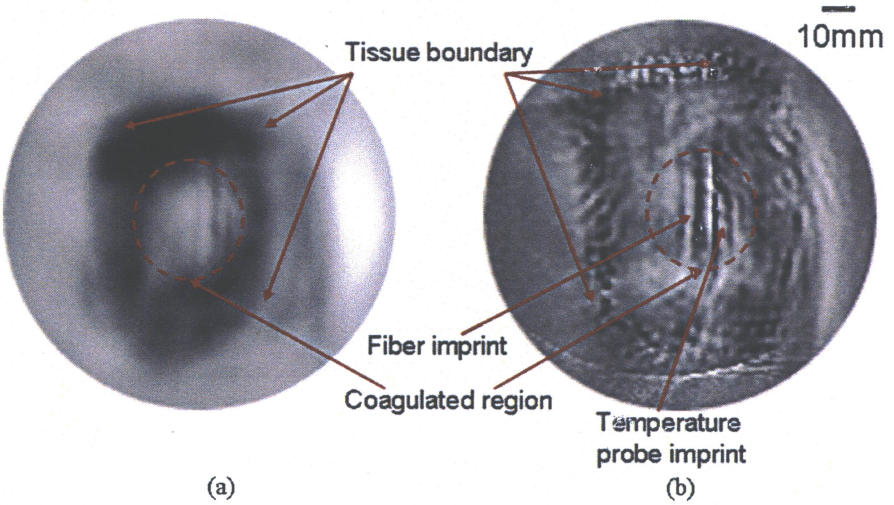

Figure 3-11: PA image depicting the thermal lesion in Figure 3-10

moving average technique and a Fourier-based digital highpass filter to remove unwanted frequency content greater that the 6dB cutoff of the transducer.

The tissue experiments illustrate the capability of PAT but also demonstrate the complex and highly variable process in detecting thermal lesions in tissue. Further research is required to obtain more quantitative results for monitoring thermal lesions and an automated technique to pre-process the data to achieve the best images. Coagulation changes the mechanical properties in tissue, reflected by a change in the Grüneisen parameter, Γ, which in turn, affects the PA signals.

3.5 Selective Imaging

Selective imaging using PAT refers to preferentially imaging structures with wavelength specific optical absorption while not being limited by the strong scattering inherent in tissues. Since PA images highly depend on the optical absorption in tissue, it

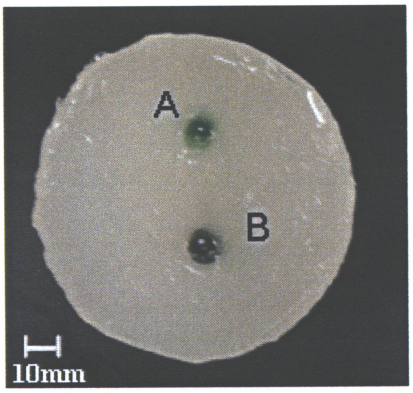

Figure 3-12: Phantom with two ~8mm diameter targets. Target A is mixed with Naphthol Green B and target B is mixed with India Ink

is possible to selectively target specific structures that possess certain optical characteristics. Useful information like oxygen saturation and total hemoglobin concentration can be obtained by this technique [69].

By preferentially varying the wavelength of light a structure can be highlighted depending on its optical absorption characteristics i.e. high versus low absorption at a particular wavelength. This is demonstrated by embedding two targets into a turbid gelatin phantom containing two dyes with different absorption spectra. Target A contains Naphthol Green B (Sigma, St. Louis, MO, USA) and target B contains India Ink as shown in Figure 3-12. The absorption characteristics of the targets measured using the DIS system are shown in Figure 3-13.

The absorption of India Ink gradually decreases with increased wavelength with a ~12% decrease in absorption between 730nm and 950nm. In contrast, Naphthol Green B absorption peaks around 740nm and then rapidly decreases to ~31% of peak between 730nm and 950nm. To investigate the effectiveness of selective PAT, light is delivered in incremental wavelengths of 20nm from 730nm – 950nm and the response of the PA

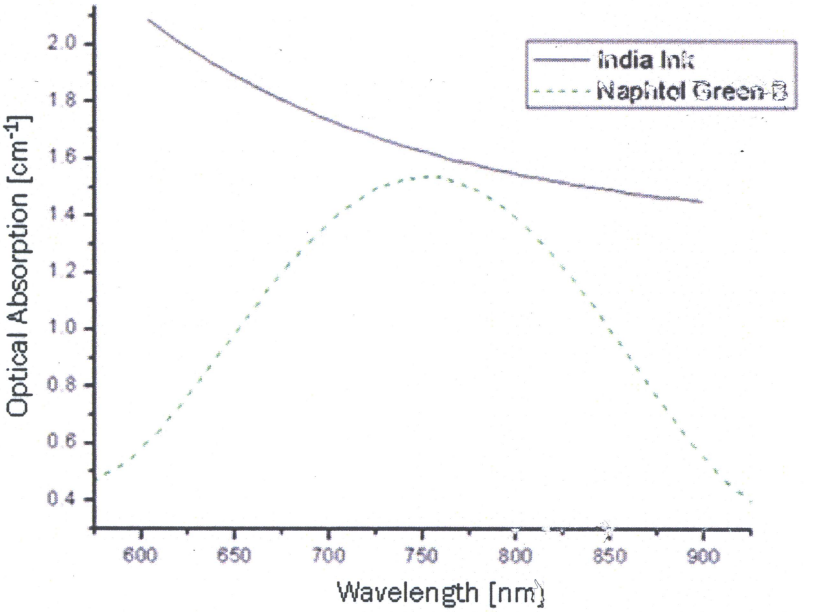

Figure 3-13: Optical Absorption Coefficient (μ_a) of India Ink (solid line) and Naphthol Green B (dotted line) used in the phantom shown in Figure 3-12

pressure transients created by the targets due their optical absorption is detected and imaged using a 1MHz transducer.

The normalized PA signals for select wavelengths are shown in Figure 3-14. All signals are recorded at the same position with the transducer directly below target B. In this position the first N-shaped signal created by target B and the second signal is created by target A. The signal produced by target A, shows a decrease in amplitude with increased wavelength illumination. This translates to a decrease in image contrast.

Figure 3-15 shows the PA reconstructed images from 730nm – 950nm with the Naphthol Green B target on top. The reconstructed images correlate well with the location and size of the targets. In addition, the differences in optical absorption spectra of the targets can be easily visualized in the images using this technique. As expected at 730nm, both targets are easily detected. However, as the wavelength of light increases, the contrast between target A and the background decreases. This is expected as the

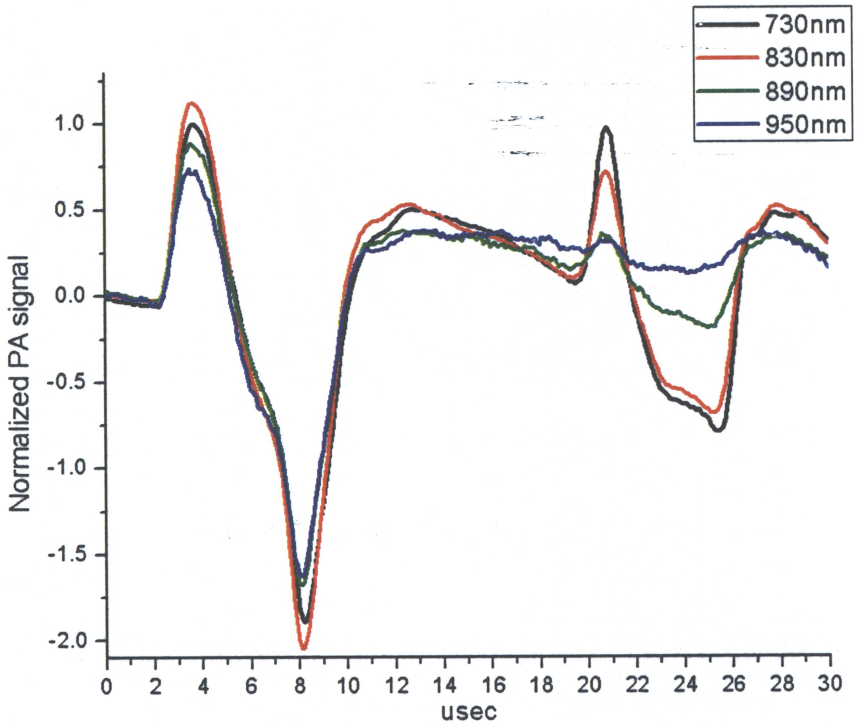

Figure 3-14: Normalized PA signals recorded with the transducer positioned directly below target B. The first N-shaped signal is created by target B and followed by the second signal created by target A. With longer wavelengths the PA signal produced by the Naphthol Green target is greatly reduced.

optical absorption by target A decreases at higher wavelengths producing a weaker PA signal.

The image reconstruction algorithm effectively normalizes the signal when converting signal amplitude to a pixel value, therefore, the difference in contrast can be quantitatively compared within each image. When different images are evaluated, the pixel values cannot be compared since they are a relative measure of the signals acquired during a specific imaging procedure. Comparing the different images has errors associated with the process, however, since the same phantom is imaged using different wavelengths and the fluence field incident on the phantom is kept constant, the images can be compared visually. The maximum difference in pixel intensity between images is approximately 12%. This is because the target containing India Ink decreases in optical

absorption by ~12% between 730nm – 950nm (Figure 3-13) and is used as the reference signal in every image reconstruction since the signal amplitude of this target is the largest. The background in the images also changes in intensity due to the absorption characteristics of gelatin and water as a function of wavelength. As mentioned in Section 2.7, the optical absorption of the background is at least a magnitude lower than the targets and is therefore ignored.

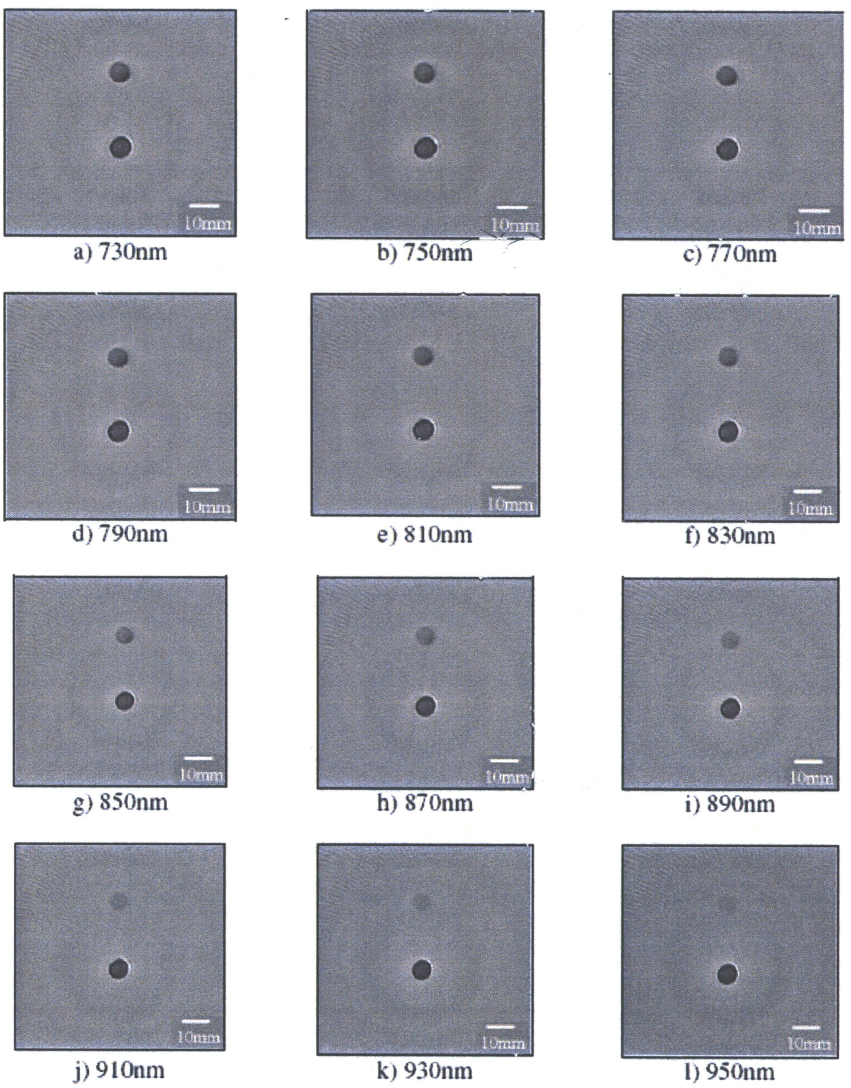

Figure 3-15: Demonstration of selective imaging using PAT. Reconstructed images with laser illumination ranging from 730nm – 950nm with the Naphthol Green B target on top and India Ink on the bottom. The dark pixels denote greater optical absorption.

3.6 Real Time Monitoring of Thermal Therapy

Tissue damage can be quantified in terms of equivalent time exposure at 43°C given by an exponential time-temperature relationship, t_{43}, and is known as thermal dose (see Section 1.7). It is described by the equivalent time it would take to produce the same biological damage if it is exposed at 43°C using any arbitrary time-temperature profile determined by Equation (1.10). For example, an exposure at 1 minute at 43°C is equivalent to 0.5 minutes at 44°C and equivalent to 0.25 minutes at 45°C etc.

Tissue mimicking albumen cylindrical phantoms 5cm in diameter and 3cm in height are fabricated as described in Section 2.8. A thermocouple is inserted at the centre and the phantom is then enclosed in a waterproof container and heated in a water bath at 70°C. When the centre reaches 70°C, the phantom is immediately cooled by placing it into another water bath at room temperature. A typical heating/cooling profile is shown in

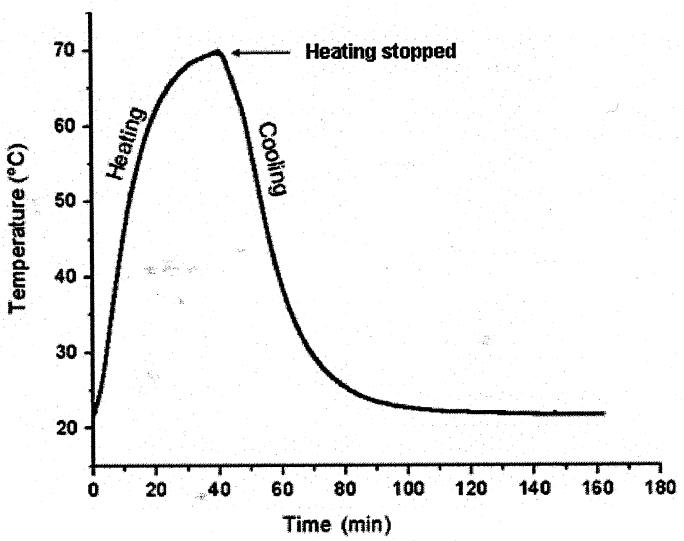

Figure 3-16: Temperature profile of albumen phantom measured at the centre while submerged in a water bath at 70°C

Figure 3-16 and the resulting thermal dose, t_{43}, at the centre of the phantom is calculated to be 6.16 x 10^{10} equivalent minutes. It should be noted that thermal dose is a measure that, in its strictest sense, is used when quantifying heat damage to living cells. However, the parallel processes that occur during the denaturing of albumen, provides large similarities that make it an acceptable approximation to use the measure of thermal dose for this study.

To examine how the structural changes of the albumen phantoms affect the PA signals, nine albumen phantoms are made, heated in 70°C water and then cooled to room temperature. Five minute heating intervals are used from five minutes to forty minutes. Using the measured heating/cooling profiles, thermal dose for all phantoms are calculated using the time-temperature curve according to Equation(1.10). The results of thermal dose for all phantoms are shown in Table 3-3.

Table 3-4 shows the optical properties of the phantoms used in experiment 3 (Figure 3-18(c)) as measured by the DIS system. When heated, the albumen coagulates causing the phantom to turn white as seen in Figure 2-8; this is also observed in the DIS data as an increase in optical scattering by a factor of 11. The dominant contributor to

Minutes Heated	Max Temperature (°C)	Thermal Dose (eq. min)
0	21	0
5	31.7	0.08
10	45.6	547.92
15	55.5	5.49×10^5
20	61.7	5.42×10^7
25	65.4	7.65×10^8
30	67.7	7.00×10^9
35	68.9	2.34×10^{10}
40	69.7	6.16×10^{10}

Table 3-3: Thermal dose, t_{43} (equivalent minutes at 43°C), for nine time-temperature exposures

Minutes Heated	μ_a [cm^{-1}]	μ_s [cm^{-1}]	μ_{eff} [cm^{-1}]
0	1.11	10.35	2.67
5	1.12	15.17	2.97
10	1.20	23.01	3.55
15	1.22	40.44	4.38
20	1.30	67.69	5.60
25	1.36	126.00	7.54
30	1.48	135.29	8.16
35	1.58	151.62	8.91
40	1.60	170.77	9.46

Table 3-4: Optical Properties of albumen phantoms at 740nm with varying thermal dose measured using the DIS system.

absorption is Naphthol Green B and, therefore, the DIS absorption spectrum qualitatively possesses the same characteristic shape as in Figure 3-13 (albumen in its native state has minimal absorption in the NIR window [75]). When measured using the DIS system at 740nm, μ_a, increased by 44% due to heating. The effective attenuation coefficient, μ_{eff}, rose three fold primarily due to the large increase in scattering.

To determine how these changes influence the PA signal, samples ~10mm in diameter are bored from the centre of each phantom to minimize the effects of gradient heating (i.e. the edges of the phantoms would have a higher thermal dose than the centre). The PA signals are produced by illuminating the samples at 740nm and the PA transients are detected by using a 1MHz transducer. Another experiment using an illumination wavelength of 810nm produced very similar results, therefore only data at 740nm are presented here. Twelve measurements are taken from around the phantom separated by 30° step increments. The twelve signals are averaged to produce one signal per phantom by aligning the data from all 12 measurements with respect to the positive peak. The experiment that is explained in this text, was not conducted in real-time, however, it can

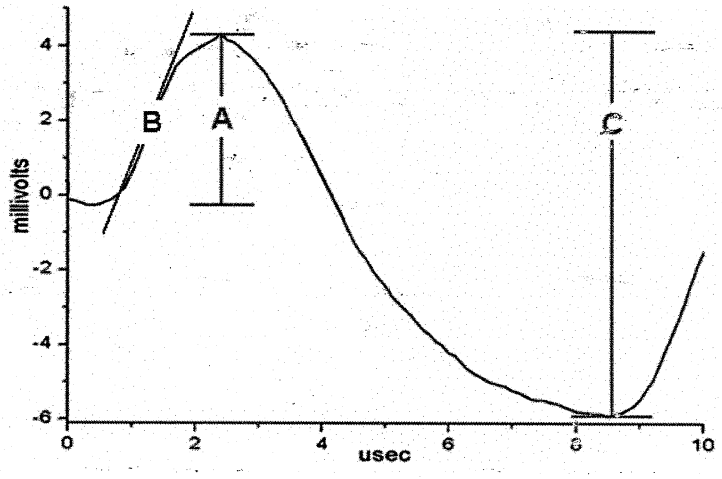

Figure 3-17: Typical photoacoustic signal denoting features analyzed. A: amplitude of the positive peak, B: the slope of the rising positive peak and C: signal peak to peak difference

be done in this manner with minor changes to the experimental procedure. To investigate the affect of thermal dose on PA signals, three specific characteristics of the signals are examined: (i) the positive peak amplitude, (ii) the slope of the rising positive peak and (iii) the peak to peak difference of the PA signal, denoted by A, B and C in Figure 3-17 respectively.

To improve readability, the averaged PA signals are displayed by also aligning the positive peaks from each phantom. Figure 3-18 shows the PA signals from three independent experiments with aligned peaks. Several observations can be made: (i) there is in initial increase in the positive peaks of the PA signal up to 10 minutes of heating and then, the positive peaks decrease with increased thermal dose as shown in Figure 3-19; (ii) the slopes of the PA signals also increase until 10 minutes of heating, and then decrease with increasing thermal dose as in Figure 3-20; and (iii) up to 10 minutes of heating, the signal peak to peak amplitudes increase. At this point there is a decrease in peak to peak amplitudes until 25 minutes, after which this difference once again increases until 40 minutes of heating as shown in Figure 3-21.

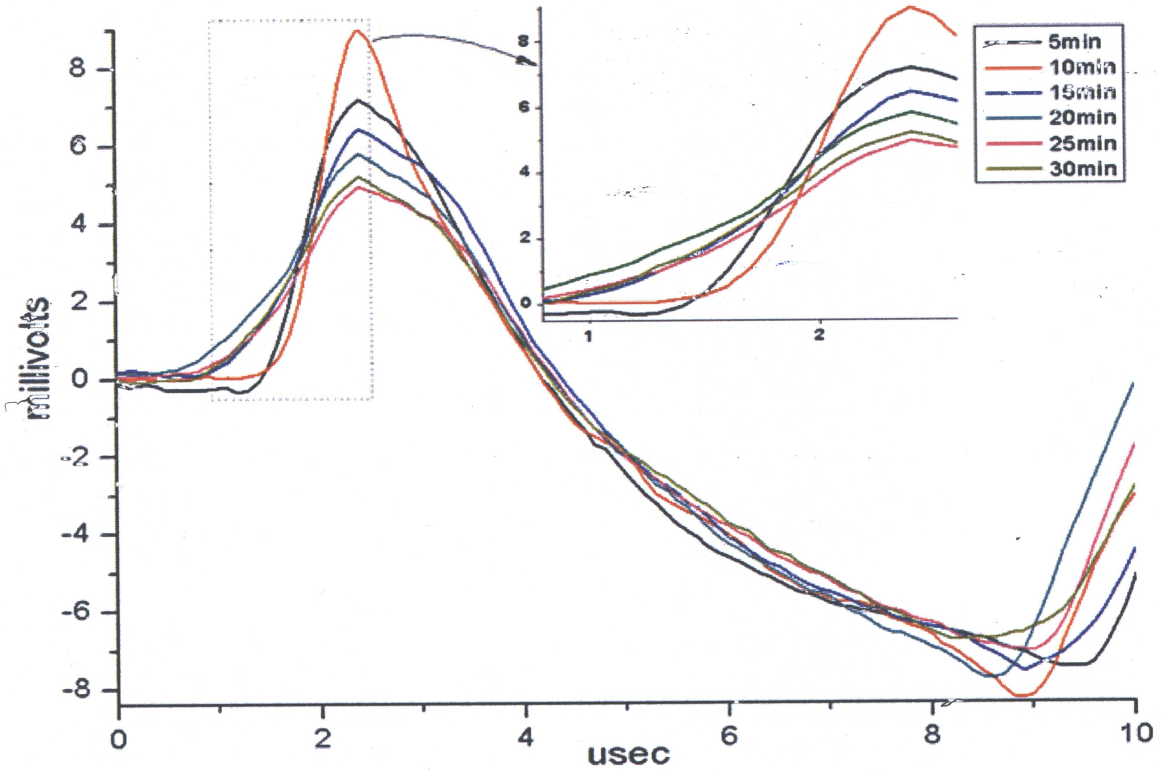

(a) Experiment 1

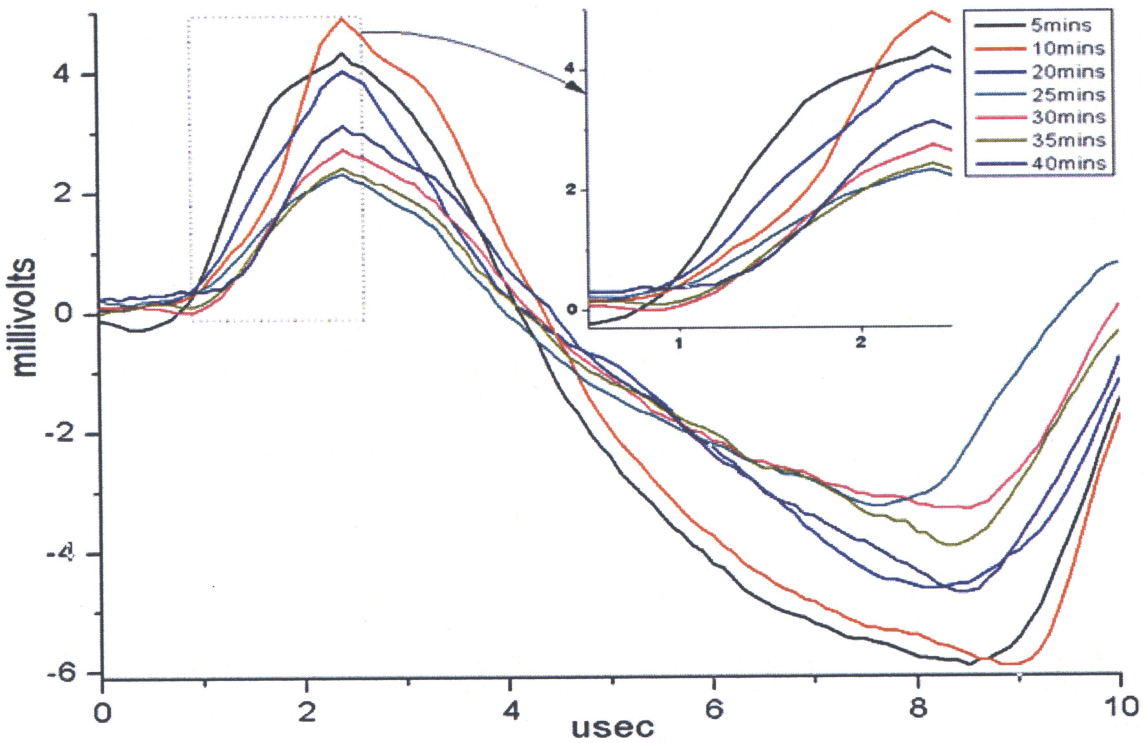

(b) Experiment 2

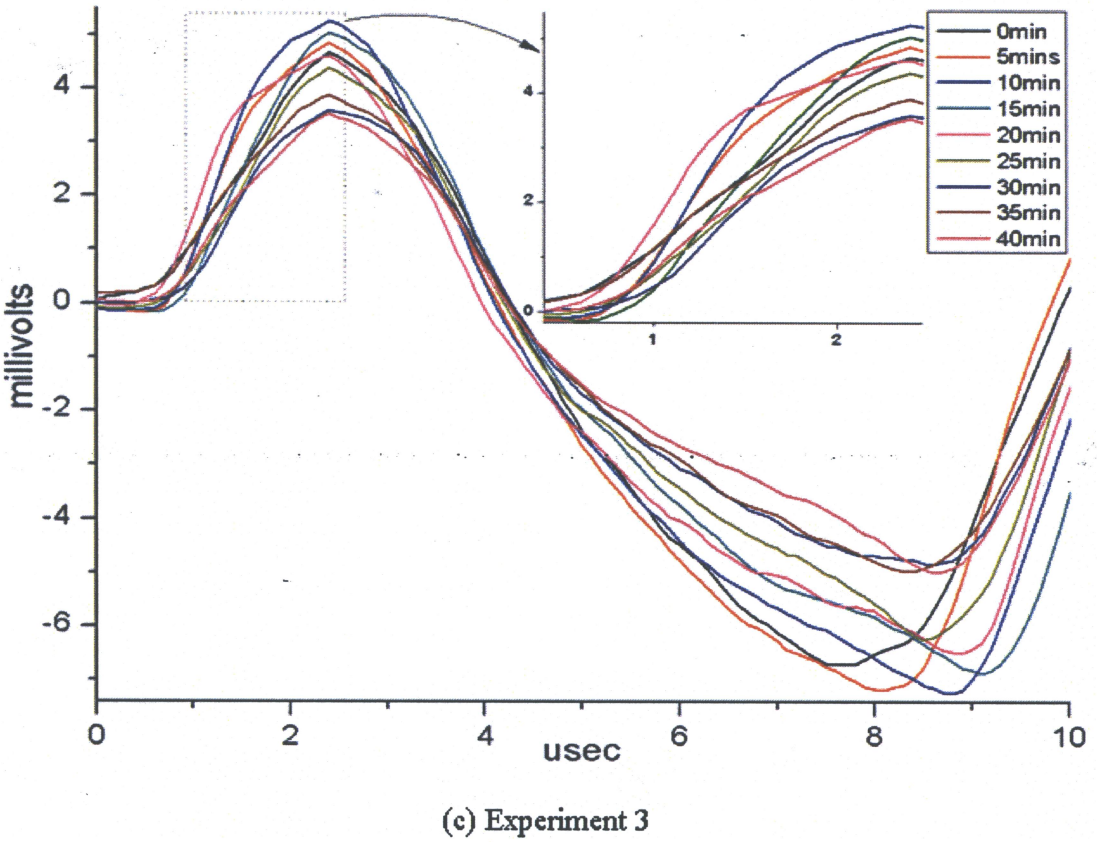

Figure 3-18: PA signals of three independent experiments showing the relationship between the PA signals and thermal dose. All figures have the positive peaks aligned and the insets are magnified regions of interest of the signals from each experiment.

The induced pressure transients (i.e. PA signals) are proportional to the product of the optical fluence, the Grüneisen parameter, Γ, and the optical absorption, μ_a (see Equation(1.7)). The observed changes in the PA signals is a result of the interplay between the optical absorption and the Grüneisen parameter, since the fluence field incident on the phantom is approximately the same for all experiments. Noticeable from Figure 3-18 is the behaviour of the PA signal during the first ten minutes of heating. During this time, there is an increase in all three characteristics analyzed. With the maximum temperature reaching 45.6°C (Table 3-3) at the centre of the phantom

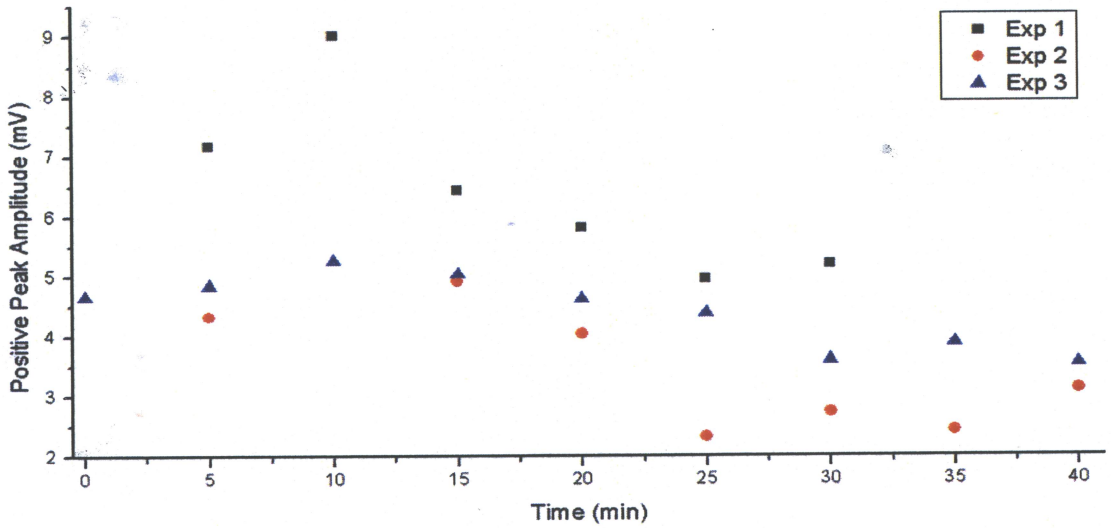

Figure 3-19: Positive PA peak signal amplitude as a function of heating in minutes

at 10 minutes of heating, a very low percentage of albumen has denatured, since the process of protein denaturing only beings around 45°C [79]. However, in the same time period, optical absorption (Table 3-4) increases by ~8%. The increase in the PA signals during the first 10 minutes of heating may be therefore attributed to the increase in the optical absorption because the percentage of denatured protein would be very low.

After 10 minutes of heating, the denaturing of albumen causes a decrease in the positive rising peak, the slope and the peak to peak difference. Even though optical absorption of the phantoms increase with thermal dose, a proportional increase in the PA signal strength (which would be expected) is not observed experimentally. A possible explanation for this result can be due to the large change in optical properties caused by heating. The increased scattering changes the fluence field inside the sample producing a different optical distribution in the phantom. This, in turn, may lower the generation of PA signals due to the lack of light penetration into the sample.

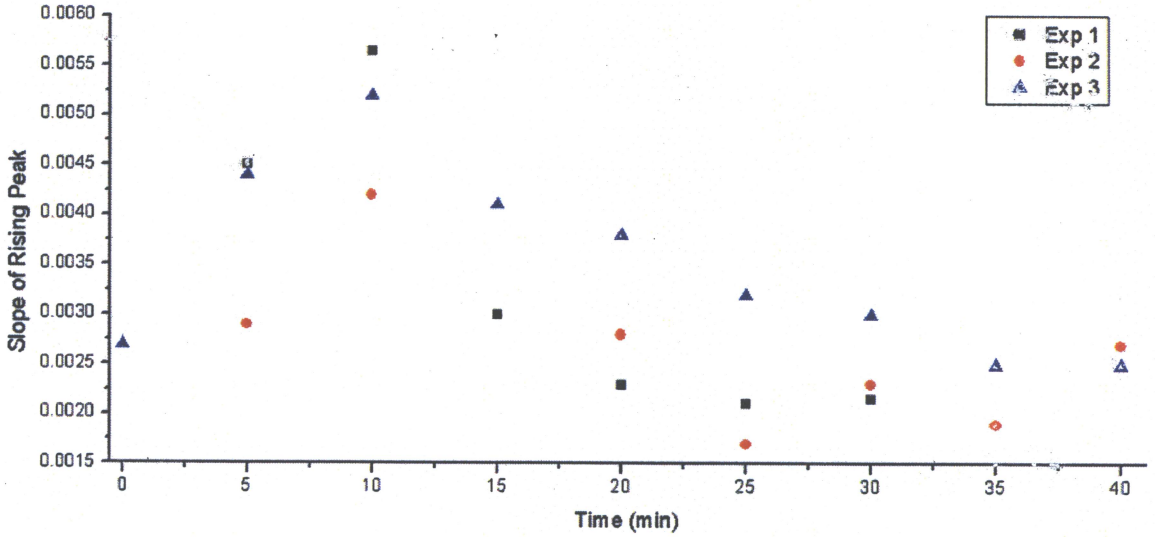

Figure 3-20: PA slope of rising peak as a function of heating in minutes

The PA signal generation is also influenced by the mechanical changes that occur during coagulation, characterized by the Grüneisen parameter. The Grüneisen parameter in water increases with higher temperature (equation(1.9)). However, it has also been shown by *Larina et al*, that even though a sample is allowed to cool to room temperature, as in our experiments, the affect of coagulation causes the Grüneisen parameter to increase [22]. This could be the cause for the increase in the peak to peak difference after 25 minutes of heating. With optical scattering at 25 minutes of heating being $125cm^{-1}$, it is possible that increasing the optical scattering to $170cm^{-1}$, at 40 minutes of heating, does not drastically alter the light distribution inside the phantoms. Therefore, an increase in the peak to peak difference after 25 minutes may be attributed to an increase in the Grüneisen parameter. Further investigation is warranted. This contribution of the Grüneisen parameter manifests itself later, only after the dominant affect of the rapidly changing optical properties have reached a plateau.

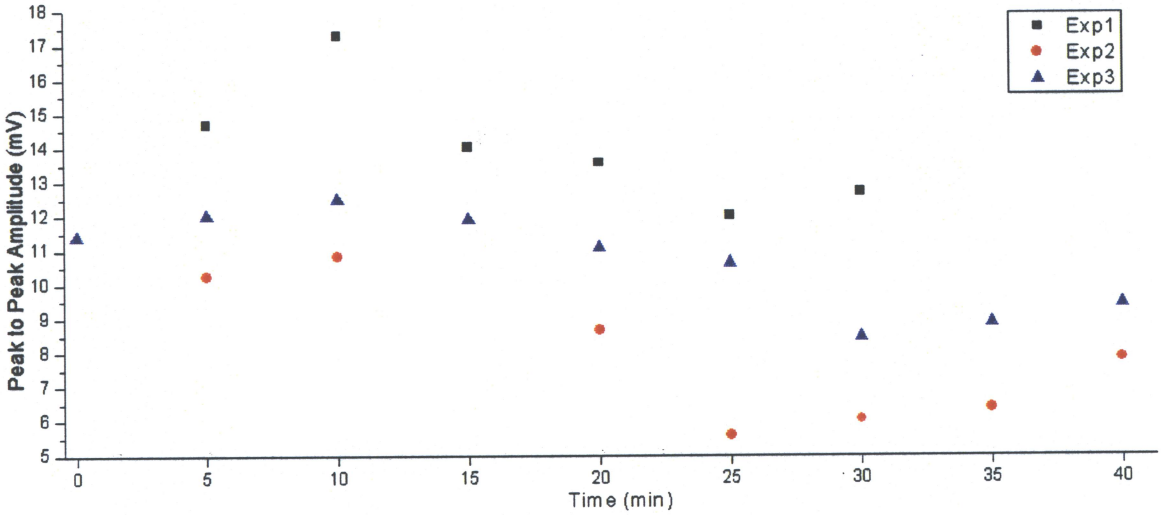

Figure 3-21: Peak to peak PA signal difference as a function of heating in minutes

It is interesting to note that the optical and mechanical properties vary at different rates and at different times during heating. By interpreting these variations and how they influence the PA signals at different stages during heating, it is possible to use this technique to monitor the progression of coagulation in albumen. This demonstrates the potential for real-time monitoring of tissue coagulation during TT.

3.7 Summary

This chapter demonstrated the potential of using PA imaging to detect, image and monitor thermal damage by showing how PA signals are affected by coagulation. Since PA signals are sensitive to variations in both the optical and mechanical properties of tissue, changes to these parameters modify the PA signals, thereby differentiating the coagulated regions from the surrounding native tissue.

The ability to image native and coagulated tissue using PAT was demonstrated using gelatin phantoms with targets prepared having optical properties similar to native and coagulated prostate tissue. After verifying that the PA system was sensitive to the low optical absorption values of prostate (μ_a ~0.6cm^{-1}), lesions in bovine muscle tissue and bovine liver were imaged.

Selective imaging was demonstrated by varying the wavelength of light to image two embedded targets in a gelatin phantom containing two different dyes with different absorption profiles. Image contrast was then manipulated simply by selecting a wavelength where a target would have high absorption – creating a larger PA signal and therefore greater contrast after image reconstruction.

Finally, the capability of using PA signals to monitor TT was shown using albumen phantoms that mimicked prostate tissue. As shown, with higher thermal dose there is a change in the characteristics of the PA signal. A correlation between the thermal dose and the PA signals is also discussed, however further work is needed to determine how the interplay of the optical and mechanical properties contribute to the change in the signal during TT.

4 Summary and Future Work

4.1 Conclusions

This work demonstrated the feasibility of PAT and real-time PA monitoring by using a single transducer prototype system to detect low absorbing targets (μ_a ~0.6cm^{-1}) embedded in turbid media and thermal lesions in tissue. It also showed that it is suitable for detecting or monitoring tumour growth or angiogenesis since it is possible to non-invasively detect deeply embedded structures in tissue at multiple time points using intrinsic tissue contrast that can be manipulated using different illumination wavelengths.

To optimize PAT for imaging two main areas were considered (i) the excitation source and (ii) the detection hardware. The excitation source used was in the NIR window because it penetrates deeply into tissue while ultrasonic transducers detected the pressure waves generated. The choice of transducer is important since the acoustic frequencies produced by the PA effect are dependent on the sizes of the targets. In the case of detecting targets ~7mm in diameter, a transducer with a centre frequency of 1MHz was sufficient and hence used.

The ability to prepare phantoms with known optical properties provided an alternative method to test the feasibility of PAT by producing controlled samples for investigating the propagation/absorption of light and the generation of PA waves with high repeatability.

Selective imaging was also demonstrated by varying the wavelength of light to preferentially target structures that possess certain optical characteristics which in turn create high image contrast. This occurs because the PA images reflect the optical heterogeneity of the sample and so it is possible to selectively target specific structures that possess certain optical characteristics while ignoring others.

The capability of using PA to monitor TT was demonstrated by showing that with higher thermal dose there is a change in the characteristics of the PA signal. The same change in signal characteristics is observed in three independent experiments using different phantoms. A correlation between the PA signal and thermal dose exists however further investigation is needed to understand the changes that occur. Nevertheless, the variation in the PA signals during tissue coagulation demonstrates the real time capability of this modality to monitor TT and can be used to quickly indicate the progression of treatment.

The possibility of using PAT to potentially image deep vasculatures implies that PAT has the ability to produce high image contrast due to the increased blood associated in tissue structures. This modality also shows promise in real time monitoring of TT however, more research is required to understand how the mechanical changes associated with tissue coagulation affect the PA signal.

4.2 Future Work

The following summarizes some key areas where further investigating is needed to improve PA imaging and the ability to better monitor TT:

1) Determine the spatial profile of the laser beam. By knowing the characteristics of the fluence field before entering the sample and it can be possible to correct for inhomogeneities using software algorithms that model the light distribution as it enters the tissue to compensate for the differences in the fluence field, i.e. the reconstructed image can be improved.
2) Devise a reconstruction algorithm that produces quantitative information. A quantitative algorithm will be a challenging task, however, if the distribution of the fluence field is known and if the one can calibrate the reconstructed image with specific targets of known optical properties, it will be possible to reconstruct an image from PA signal data that can display quantitative information.
3) Understand the effect of the Grüneisen parameter on tissue during TT. Temperature affects the Grüneisen parameter and this increase will also proportionally affect the PA signal. Knowing how the Grüneisen parameter influences the PA signal during temperature change will help in the monitoring of TT.
4) Conduct further experiments to understand the ability in monitoring TT using PA imaging with *ex vivo* native and thermally coagulated human tissue experiments to understand the detection parameters using PA imaging.
5) Revise the experimental protocol of real time PA monitoring to measure the PA signals caused by thermal induced coagulation *during* heating. By acquiring PA data while heating a sample, the experiment will simulate a more realistic treatment scenario thereby the PA data will more closely represent what could be expected during TT.

6) Conduct experiments on animal models to observe how the PA signal is affected by absorption of light due to skin and the ability of image below the skin. Also needed, will be to investigate the ability to differentiate thermal lesions using TT *in vivo*.

References

[1] A. B. Bell, "On the production and reproduction of sound by light," *Am. J. Sci.,* vol. 20, p. 305, 1880.

[2] V. E. Gusev and A. A. Karabutov, *Laser Optoacoustics* New York: AIP, 1993.

[3] A. A. Oraevsky and A. A. Karabuto, "Optoacoustic tomography," in *Biomedical Photonics Handbook,* T. Vo-Dinh, Ed. New York: CRC, 2003, pp. 34.1-34.34.

[4] C. K. N. Patel and A. C. Tam, "Pulsed optoacoustic spectroscopy of condensed matter," *Reviews of Modern Physics,* vol. 53, p. 517, 1981.

[5] D. Hutchins and A. C. Tam, "Pulsed Photoacoustic Materials Characterization," *Ultrasonics, Ferroelectrics and Frequency Control, IEEE Transactions on,* vol. 33, pp. 429-449, 1986.

[6] A. Mandelis, "Principles and Perspectives of Photothermal and Photoacoustic Phenomena," New York: Elsevier Science, 1992.

[7] G. J. Diebold and T. Sun, "Properties of Photoacoustic Waves in One, Two, and Three Dimensions," *Acoustica,* vol. 80, 1994.

[8] L. V. Wang and H.-i. Wu, *Biomedical Optics: Principles and Imaging*: Wiley, 2007.

[9] A. Rosencwaig, *Photoacoustics and photoacoustic spectroscopy.* Malabar: Robert E.Krieger Publishing Inc., 1990.

[10] V. G. Andreev, A. A. Karabutov, and A. A. Oraevsky, "Detection of ultrawide-band ultrasound pulses in optoacoustic tomography," *Ieee Transactions on Ultrasonics Ferroelectrics and Frequency Control,* vol. 50, pp. 1383-1390, Oct 2003.

[11] W. F. Cheong, S. A. Prahl, and A. J. Welch, "A review of the optical properties of biological tissues," *Quantum Electronics, IEEE Journal of,* vol. 26, pp. 2166-2185, 1990.

[12] S. L. Jacques and S. A. Prahl, "Absorption spectra for biological tissues, http://omlc.ogi.edu/classroom/ece532/class3/muaspectra.html," 1998.

[13] B. C. Wilson, "Optical properties of tissues," in *Encyclopedia of human biology.* vol. 5, R. Dulbecco, Ed. San Diego: Academic Press, 1991, pp. 587-597.

[14] P. Parsa, S. L. Jacques, and N. S. Nishioka, "Optical properties of rat liver between 350 and 2200 nm," *Applied Optics,* vol. 28, pp. 2325-2330, 1989.

[15] P. Fish, *Physics and instrumentation of diagnostic medical ultrasound.* New York: Wiley, 1990.

[16] F. A. Duck, *Physical Properties of Tissues: A Comprehensive Reference Book.* London: Academic Pr, 1990.

[17] P. N. T. Wells, "Ultrasonic imaging of the human body," *Reports on Progress in Physics,* vol. 62, pp. 671-722, 1999.

[18] R. S. C. Cobbold, *Foundations of Biomedical Ultrasound.* USA: Oxford University Press, 2006.

[19] *American National Standard for the Safe Use of Lasers in Health Care Facilities: Standard Z136.1-2000* New York: ANSI Inc, 2000.

[20] A. A. Oraevsky, S. L. Jacques, and F. K. Tittel, "Measurement of tissue optical properties by time-resolved detection of laser-induced transient stress," *Applied Optics,* vol. 36, pp. 402-415, 1997.

[21] A. A. Oraevsky, S. L. Jacques, and F. K. Tittel, "Determination of tissue optical properties by piezoelectric detection of laser-induced stress waves," in *Proceedings of SPIE - The International Society for Optical Engineering*, Los Angeles, CA, USA, 1993, pp. 86-101.

[22] K. V. Larin, I. V. Larina, M. Motamedi, and R. O. Esenaliev, "Optoacoustic laser monitoring of cooling and freezing of tissues," *Quantum Electronics,* vol. 32, pp. 953-958, 2002.

[23] Y. Fan, A. Mandelis, G. Spirou, and I. A. Vitkin, "Development of a laser photothermoacoustic frequency-swept system for subsurface imaging: Theory and experiment," *Journal of the Acoustical Society of America,* vol. 116, pp. 3523-3533, 2004.

[24] G. Ku, X. Wang, X. Xie, G. Stoica, and L. V. Wang, "Imaging of tumor angiogenesis in rat brains in vivo by photoacoustic tomography," *Applied Optics,* vol. 44, pp. 770-775, 2005.

[25] A. A. Oraevsky, E. V. Savateeva, S. V. Solomatin, A. A. Karabutov, V. G. Andreev, Z. Gatalica, T. Khamapirad, and P. M. Henrichs, "Optoacoustic imaging of blood for visualization and diagnostics of breast cancer," in *Proceedings of SPIE - The International Society for Optical Engineering*, San Jose, CA, 2002, pp. 81-94.

[26] C. G. A. Hoelen, F. F. M. De Mul, R. Pongers, and A. Dekker, "Three-dimensional photoacoustic imaging of blood vessels in tissue," *Optics Letters,* vol. 23, pp. 648-650, 1998.

[27] A. A. Oraevsky, V. A. Andreev, A. A. Karabutov, D. R. Fleming, Z. Gatalica, H. Singh, and R. O. Esenaliev, "Laser opto-acoustic imaging of the breast: detection of cancer angiogenesis," in *Proceedings of SPIE - The International Society for Optical Engineering*, San Jose, CA, USA, 1999, pp. 352-363.

[28] R. A. Kruger, W. L. Kiser, D. R. Reinecke, G. A. Kruger, and K. D. Miller, "Thermoacoustic molecular imaging of small animals," *Molecular Imaging,* vol. 2, pp. 113-123, 2003.

[29] X. Wang, Y. Pang, G. Ku, G. Stoica, and L. V. Wang, "Three-dimensional laser-induced photoacoustic tomography of mouse brain with the skin and skull intact," *Optics Letters,* vol. 28, pp. 1739-1741, 2003.

[30] J. Mobley and T. Vo-Dinh, "Biomedical Photonics Handbook," T. Vo-Dinh, Ed. Boca Raton, FL: CRC, 2003.

[31] K. R. Foster, "Thermal and nonthermal mechanisms of interaction of radio-frequency energy with biological systems," *Plasma Science, IEEE Transactions on,* vol. 28, pp. 15-23, 2000.

[32] P. C. Beard and T. N. Mills, "2D line-scan photoacoustic imaging of absorbers in a scattering tissue phantom," in *Proceedings of SPIE - The International Society for Optical Engineering*, San Jose, CA, 2001, pp. 34-42.

[33] C. G. A. Hoelen and F. F. M. De Mul, "Image reconstruction for photoacoustic scanning of tissue structures," *Applied Optics,* vol. 39, pp. 5872-5883, 2000.

[34] A. A. Karabutov, E. V. Savateeva, and A. A. Oraevsky, "Optoacoustic supercontrast for early cancer detection," in *Proceedings of SPIE - The International Society for Optical Engineering*, San Jose, CA, 2001, pp. 179-187.

[35] K. P. Kostli, D. Frauchiger, J. J. Niederhauser, G. Paltauf, H. P. Weber, and M. Frenz, "Optoacoustic imaging using a three-dimensional reconstruction algorithm," *IEEE Journal on Selected Topics in Quantum Electronics,* vol. 7, pp. 918-923, 2001.

[36] S. Manohar, A. Kharine, J. C. G. van Hespen, W. Steenbergen, and T. G. van Leeuwen, "Photoacoustic mammography laboratory prototype: Imaging of breast tissue phantoms," *Journal of Biomedical Optics,* vol. 9, pp. 1172-1181, 2004.

[37] G. Paltauf, H. Schmidt-Kloiber, K. P. Kostli, and M. Frenz, "Optical method for two-dimensional ultrasonic detection," *Applied Physics Letters,* vol. 75, pp. 1048-1050, 1999.

[38] G. Paltauf, J. A. Viator, S. A. Prahl, and S. L. Jacques, "Iterative reconstruction algorithm for optoacoustic imaging," *Journal of the Acoustical Society of America,* vol. 112, pp. 1536-1544, 2002.

[39] X. Wang, Y. Xu, M. Xu, S. Yokoo, E. S. Fry, and L. V. Wang, "Photoacoustic tomography of biological tissues with high cross-section resolution: Reconstruction and experiment," *Medical Physics,* vol. 29, pp. 2799-2805, 2002.

[40] G. Ku and L. V. Wang, "Scanning microwave-induced thermoacoustic tomography: Signal, resolution, and contrast," *Medical Physics,* vol. 28, pp. 4-10, 2001.

[41] K. P. Kostli, M. Frenz, H. Bebie, and H. P. Weber, "Temporal backward projection of optoacoustic pressure transients using Fourier transform methods," *Physics in Medicine and Biology,* vol. 46, pp. 1863-1872, 2001.

[42] M. Xu, Y. Xu, and L. V. Wang, "Time-domain reconstruction algorithms and numerical simulations for thermoacoustic tomography in various geometries," *IEEE Transactions on Biomedical Engineering,* vol. 50, pp. 1086-1099, 2003.

[43] Y. V. Zhulina, "Optimal statistical approach to optoacoustic image reconstruction," *Applied Optics,* vol. 39, pp. 5971-5977, 2000.

[44] R. A. Kruger, W. L. Kiser Jr, D. R. Reinecke, and G. A. Kruger, "Thermoacoustic computed tomography using a conventional linear transducer array," *Medical Physics,* vol. 30, pp. 856-860, 2003.

[45] R. A. Kruger, P. Liu, Y. R. Fang, and C. R. Appledorn, "Photoacoustic ultrasound (PAUS) - Reconstruction tomography," *Medical Physics,* vol. 22, pp. 1605-1609, 1995.

[46] R. A. Kruger, K. D. Miller, H. E. Reynolds, W. L. Kiser Jr, D. R. Reinecke, and G. A. Kruger, "Breast cancer in vivo: Contrast enhancement with thermoacoustic CT at 434 MHz - Feasibility study," *Radiology,* vol. 216, pp. 279-283, 2000.

[47] R. A. Kruger, K. Stantz, and W. L. Kiser Jr, "Thermoacoustic CT of the breast," in *Proceedings of SPIE - The International Society for Optical Engineering*, San Diego, CA, 2002, pp. 521-525.

[48] R. O. Esenaliev, A. A. Karabutov, and A. A. Oraevsky, "Sensitivity of laser opto-acoustic imaging in detection of small deeply embedded tumors," *IEEE Journal on Selected Topics in Quantum Electronics,* vol. 5, pp. 981-988, 1999.

[49] A. A. Oraevsky, A. A. Karabutov, S. V. Solomatin, E. V. Savateeva, V. G. Andreev, Z. Gatalica, H. Singh, and R. D. Fleming, "Laser optoacoustic imaging of breast cancer in vivo," in *Proceedings of SPIE - The International Society for Optical Engineering*, San Jose, CA, 2001, pp. 6-15.

[50] R. G. M. Kolkman, E. Hondebrink, W. Steenbergen, T. G. van Leeuwen, and F. F. M. de Mul, "Photoacoustic imaging of blood vessels with a double-ring sensor featuring a narrow angular aperture," *Journal of Biomedical Optics,* vol. 9, pp. 1327-1335, 2004.

[51] G. M. Spirou, A. Vitkin, B. C. Wilson, W. M. Whelan, P. M. Henrichs, K. Mehta, T. Miller, A. Yee, J. Meador, and A. A. Oraevsky, "Development and testing of an optoacoustic imaging system for monitoring and guiding prostate cancer therapies," in *Progress in Biomedical Optics and Imaging*, San Jose, CA, 2004, pp. 44-56.

[52] C. Richter, G. Spirou, A. A. Oraevsky, W. M. Whelan, and M. C. Kolios, "Examination of contrast mechanisms in optoacoustic imaging of thermal lesions," in *Proceedings of SPIE - The International Society for Optical Engineering*, San Jose, CA, 2006.

[53] E. Z. Zhang, J. Laufer, and P. Beard, "Three dimensional photoacoustic imaging of vascular anatomy in small animals using an optical detection system," in *Progress in Biomedical Optics and Imaging - Proceedings of SPIE*, San Jose, CA, 2007.

[54] E. Z. Zhang and P. Beard, "Ultra high sensitivity, wideband Fabry Perot ultrasound sensors as an alternative to piezoelectric PVDF transducers for biomedical photoacoustic detection," in *Progress in Biomedical Optics and Imaging - Proceedings of SPIE*, San Jose, CA, 2004, pp. 222-229.

[55] A. J. Welch, M. Motamedi, S. Rastegar, G. L. LeCarpentier, and D. Jansen, "Laser thermal ablation," *Photochemistry and Photobiology,* vol. 53, pp. 815-823, 1991.

[56] S. G. Bown, "Phototherapy of tumors," *World Journal of Surgery,* vol. 7, pp. 700-709, 1983.

[57] M. A. Hall-Craggs and J. S. Vaidya, "Minimally invasive therapy for the treatment of breast tumours," *European Journal of Radiology,* vol. 42, pp. 52-57, 2002.

[58] F. Izzo, "Other thermal ablation techniques: Microwave and interstitial laser ablation of liver tumors," *Annals of Surgical Oncology,* vol. 10, pp. 491-497, 2003.

[59] T. F. Aho and P. J. Gilling, "Laser therapy for benign prostatic hyperplasia: A review of recent developments," *Current Opinion in Urology,* vol. 13, pp. 39-44, 2003.

[60] S. A. Sapareto and W. C. Dewey, "Thermal dose determination in cancer therapy," *International Journal of Radiation Oncology Biology Physics,* vol. 10, pp. 787-800, 1984.

[61] S. R. H. Davidson, I. A. Vitkin, M. D. Sherar, and W. M. Whelan, "Characterization of measurement artefacts in fluoroptic temperature sensors: Implications for laser thermal therapy at 810 nm," *Lasers in Surgery and Medicine,* vol. 36, pp. 297-306, 2005.

[62] J. D. Hazle, R. J. Stafford, and R. E. Price, "Magnetic resonance imaging-guided focused ultrasound thermal therapy in experimental animal models: Correlation of ablation volumes with pathology in rabbit muscle and VX2 tumors," *Journal of Magnetic Resonance Imaging,* vol. 15, pp. 185-194, 2002.

[63] R. D. Peters, E. Chan, J. Trachtenberg, S. Jothy, L. Kapusta, W. Kucharczyk, and R. M. Henkelman, "Magnetic resonance thermometry for predicting thermal damage: An application of interstitial laser coagulation in an in vivo canine prostate model," *Magnetic Resonance in Medicine,* vol. 44, pp. 873-883, 2000.

[64] A. B. Ross, C. J. Diederich, W. H. Nau, H. Gill, D. M. Bouley, B. Daniel, V. Rieke, R. K. Butts, and G. Sommer, "Highly directional transurethral ultrasound applicators with rotational control for MRI-guided prostatic thermal therapy," *Physics in Medicine and Biology,* vol. 49, pp. 189-204, 2004.

[65] L. C. L. Chin, B. C. Wilson, W. M. Whelan, and I. A. Vitkin, "Radiance-based monitoring of the extent of tissue coagulation during laser interstitial thermal therapy," *Optics Letters,* vol. 29, pp. 959-961, 2004.

[66] L. C. L. Chin, W. M. Whelan, M. D. Sherar, and I. A. Vitkin, "Changes in relative light fluence measured during laser heating: Implications for optical monitoring and modelling of interstitial laser photocoagulation," *Physics in Medicine and Biology,* vol. 46, pp. 2407-2420, 2001.

[67] A. Veltri, G. De Fazio, V. Malfitana, G. Isolato, D. Fontana, A. Tizzani, and G. Gandini, "Percutaneous US-guided RF thermal ablation for malignant renal tumors: Preliminary results in 13 patients," *European Radiology,* vol. 14, pp. 2303-2310, 2004.

[68] F. Manns, P. J. Milne, X. Gonzalez-Cirre, D. B. Denham, J. M. Parel, and D. S. Robinson, "In situ temperature measurements with thermocouple probes during laser interstitial thermotherapy (LITT): Quantification and correction of a measurement artifact," *Lasers in Surgery and Medicine,* vol. 23, pp. 94-103, 1998.

[69] M. Xu and L. V. Wang, "Photoacoustic imaging in biomedicine," *Review of Scientific Instruments,* vol. 77, pp. 041101-22, 2006.

[70] G. Ku, X. Wang, G. Stoica, and L. V. Wang, "Multiple-bandwidth photoacoustic tomography," *Physics in Medicine and Biology,* vol. 49, pp. 1329-1338, 2004.

[71] S. Park, J. Shah, S. R. Aglyamov, A. B. Karpiouk, S. Mallidi, A. Gopal, H. Moon, X. J. Zhang, W. G. Scott, and S. Y. Emelianov, "Integrated system for ultrasonic, photoacoustic and elasticity imaging," in *Progress in Biomedical Optics and Imaging - Proceedings of SPIE*, San Diego, CA, 2006.

[72] S. A. Prahl, M. J. C. van Gemert, and A. J. Welch, "Determining the optical properties of turbid media by suing the adding-doubling method," *Applied Optics,* vol. 32, pp. 559-568, 1993.

[73] A. Roggan, H. J. Albrecht, K. Doerschel, O. Minet, and G. J. Mueller, "Experimental set-up and Monte-Carlo model for the determination of optical tissue properties in the wavelength range 330 to 1100 nm," in *Laser Interaction with Hard and Soft Tissue II*: SPIE, 1995.

[74] I. V. Yaroslavsky and V. V. Tuchin, "Inverse Monte Carlo method for spectrophotometric data processing," in *Cell and Biotissue Optics: Applications in Laser Diagnostics and Therapy*, Moscow, Russia, 1994, pp. 57-68.

[75] M. N. Iizuka, M. D. Sherar, and I. A. Vitkin, "Optical phantom materials for near infrared laser photocoagulation studies," *Lasers in Surgery and Medicine,* vol. 25, pp. 159-169, 1999.

[76] M. N. Iizuka, I. A. Vitkin, M. C. Kolios, and M. D. Sherar, "The effects of dynamic optical properties during interstitial laser photocoagulation," *Physics in Medicine and Biology,* vol. 45, pp. 1335-1357, 2000.

[77] J. W. Pickering, "Optical property changes as a result of protein denature in albumen and yolk," *Journal of Photochemistry and Photobiology B: Biology,* vol. 16, pp. 101-111, 1992.

[78] G. J. Mueller and A. Roggan, "Optical properties of biological tissues in the near-infrared wavelength range: review and measurements," in *Laser-Induced Interstitial Thermotherapy*, A. Roggan, K. Dorschel, Minet, D. Wolff, and G. Muller, Eds., 1995, pp. 10–44.

[79] J. C. Bischof and X. He, "Thermal stability of proteins," *Annals of the New York Academy of Sciences.,* vol. 1066, pp. 12-33, 2005.